Oceanic Cyclogenesis as Induced by a Mesoscale Convective System Moving Offshore. Part II: Genesis and Thermodynamic Transformation

DA-LIN ZHANG AND NING BAO

Department of Atmospheric and Oceanic Sciences, McGill University, Montreal, Quebec, Canada

(Manuscript received 11 October 1995, in final form 5 April 1996)

ABSTRACT

The genesis of intense cyclonic vorticity in the boundary layer and the transformation of a low-level cold pool to a warm-core anomaly associated with the long-lived mesoscale convective systems (MCSs), which produced the July 1977 Johnstown flash flood and later developed into a tropical storm, are examined using a 90-h real-data simulation of the evolution from a continental MCS/vortex to an oceanic cyclone/storm system. It is shown that the midlevel vortex/trough at the end of the continental MCS's life cycle is characterized by a warm anomaly above and a cold anomaly below. The mesovortex, as it drifts toward the warm Gulf Stream water, plays an important role in initiating and organizing a new MCS and a cyclonic (shear) vorticity band at the southern periphery of the previously dissipated MCS. It is found from the vorticity budget that the vorticity band is amplified through stretching of absolute vorticity as it is wrapped around in a slantwise manner toward the cyclone center. Then, the associated shear vorticity is converted to curvature vorticity near the center, leading to the formation of a "comma-shaped" vortex and the rapid spinup of the surface cyclone to tropical storm intensity.

Thermodynamic budgets reveal that the vertical transfer of surface fluxes from the warm ocean and the convectively induced grid-scale transport are responsible for the development of a high-θ_e tongue, which is wrapped around in a fashion similar to the vorticity band, causing conditional instability and further organization of the convective storm. Because the genesis occurs at the southern periphery of the vortex/trough, the intensifying cyclonic circulation tends to advect the pertinent cold air in the north-to-northwesterly flow into the convective storm and the ambient warmer air into the cyclone center, thereby transforming the low-level cold anomaly to a warm-cored structure near the cyclone core. It is shown that the transformation and the evolution of the surface cyclone are mainly driven by the low-level vorticity concentrations.

It is found that many of the cyclogenesis scenarios in the present case are similar to those noted in previous tropical cyclogenesis studies and observed at the early stages of tropical cyclogenesis from MCSs during the Tropical Experiment in Mexico. Therefore, the results have significant implications with regard to tropical cyclogenesis from MCSs.

1. Introduction

In Part I (Zhang and Bao 1996), we have presented a successful 90-h simulation (i.e., from 1200 UTC 19 to 0600 UTC 23 July 1977) of an oceanic cyclogenesis event from the mesoscale convective systems (MCSs) that produced the 19–20 July 1977 Johnstown, Pennsylvania, flash flood, using the Pennsylvania State University–NCAR mesoscale model (Anthes et al. 1987; Zhang and Fritsch 1986). The model reproduces very well the life cycle of the continental MCSs (i.e., a squall line and a mesoscale convective complex or MCC) and the associated surface and midlevel perturbations (e.g., a mesolow/vortex and mesohighs) during the first 18-h integration (Zhang and Fritsch 1986, 1987; hereafter ZF86 and ZF87, respectively), the initiation of a new MCS at the southern periphery of the previously dissipated MCC after it drifted into the warm Gulf Stream water, and then the genesis of a surface mesolow by 60 h into the integration and ultimately to "tropical storm" intensity (Bosart and Sanders 1981, hereafter BS81). The oceanic cyclogenesis has been shown to be induced by the continental vortex/trough system, after it moved offshore, and subsequently driven by organized deep convection in a prefrontal, near-barotropic environment.

As a follow-up, we wish to address in this paper, through model diagnosis and budgets, the following two key issues to the understanding of oceanic cyclogenesis as induced by an MCS and then driven by deep convection:

1) What mechanisms are responsible for the transformation of an MCS with a deep cold pool in the lower troposphere into an intense mesocyclone that is characterized by a deep warm-cored structure?

2) What processes determine the amplification of lower-level cyclonic vorticity in tropical storms in re-

Corresponding author address: Dr. Da-Lin Zhang, Department of Atmospheric and Oceanic Sciences, McGill University, 805 Sherbrooke Street West, Montreal, PQ H3A 2K6, Canada.
Email: dzhang@zephyr.meteo.mcgill.ca

lation to the convectively generated midlevel mesovortex from the previously dissipated MCS?

To our knowledge, the above two issues have not been properly addressed in the previous studies owing to the limited observations over vast data-void oceans (see the recent review by Zehr 1992). For example, some of the previous studies (e.g., Davidson et al. 1990; Mapes and Houze 1993) suggested that the transformation of MCSs to tropical storms may occur when some portion of cyclonic vorticity associated with the midlevel mesovortex descends to the surface and then amplifies through vortex stretching in the presence of intensifying low-level inflows along convective bands. However, in their analyses of tropcical cyclogenesis cases during TEXMEX,[1] Emanuel et al. (1993) found the concentration of low-level high cyclonic vorticity in lines or arcs along gust fronts far away from the location of the midlevel mesovortex that is cold-cored in the lower troposphere. They proposed a conceptual model in which the low-level cold pool near the vortex core is hypothesized to be primarily reheated and moistened by surface fluxes over the warm ocean until a warm-core anomaly and new convection develop near the circulation center.

The objectives of the present paper are to (i) document the meso-β-scale structures and evolution of cyclonic vorticity associated with the oceanic cyclone/storm system (sections 2 and 3); (ii) quantify the processes responsible for the simulated structures and amplification of the cyclone through budget calculations of the vorticity (section 4) and thermodynamic (section 5) equations; and (iii) determine the importance of deep convection in the amplification of cyclonic vorticity as well as in the thermodynamic transformation (sections 2 and 5). As part of the understanding, we will also examine some important mesoscale features and their vertical kinematic and thermodynamic structures associated with the oceanic cyclogenesis.

2. Evolution of low-level cyclonic vorticity

In this section, we use the control simulation presented in Part I to diagnose the horizontal structures and evolution of the cyclonic vorticity associated with the oceanic cyclone/storm system, and in the next section we examine the relationships between the cyclone's vorticity and the midlevel mesovortex generated by the continental MCSs. For the convenience of later discussions, some selected surface maps of the MCS/cyclone development are given in Fig. 1, which are taken from 24-, 60-, 72-, and 84-h simulations, valid at 1200 UTC 20, 0000 and 1200 UTC 22, and 0000 UTC 23 July 1977 (henceforth 20/12-24, 22/00-60, 22/12-72, and 23/00-84), respectively. These four periods are chosen since they represent roughly the dissipated stage of the continental MCC, and the incipient, intensifying and mature stages of the oceanic cyclone/storm (or convective band).

Figures 2a–f show the 6-h evolution of vertical relative vorticity, superposed with (ground relative) wind vectors, at 950 hPa from 60- to 90-h integrations during which time more rapid deepening occurs (see Fig. 1). The 950-hPa level is presented because this is roughly the level at which the flow intensity and vorticity production in the cyclone/storm system are maximized. At 22/00-60, the 950-hPa mesoscale flow is generally similar to but stronger than that at the surface (cf. Fig. 9c in Part I and Fig. 2a herein), showing a broad cyclonic circulation associated with the mesovortex/trough superposed on the westerly flow. A localized vorticity center, as marked by a cross in Fig. 2a, appears at the central portion of the weak-flow region to the north of the surface mesolow, which represents the intensity of the mesovortex in the lower troposphere (i.e., the surface mesotrough). Of our concern here is the development of two concentrated vorticity (V) bands each with a width of 120–180 km (based on their greater than f magnitudes): one distributed parallel to but lagged slightly behind the convective band with its peak value close to the surface mesolow (at 150–180 km to the south of the midlevel mesovortex) and the other originating from the northeastern portion of the surface front. Because of their relations to the convective band and the large-scale front, these two V-bands could be regarded as being convectively and baroclinically driven, respectively, although the latter is persistently enhanced by deep convection ahead of the front. It is evident that the baroclinic V-band consists mostly of shear vorticity, whereas the convective V-band contains both shear and curvature vorticity associated with the convectively enhanced broad surface trough (cf. Figs. 2a and 1b). Such high V-bands have also been observed during TEXMEX in association with gust fronts at some distance from midlevel mesovortices (see Emanuel et al. 1993). We will see below that these two V-bands tend to wrap around into the cyclone center in a slantwise fashion[2] similar to the high-θ_e tongue presented in Part I (see Figs. 11c and 13c therein), as indicated by large arrows in Figs. 2a–f, and they appear to determine the evolution and intensification of the surface cyclone.

[1] Tropical Experiment in Mexico that was conducted between 1 July and 8 August 1991 to investigate tropical cyclogenesis from MCSs (see Emanuel et al. 1993). Such a phenomenon was observed in 4 of 6 intense operation periods.

[2] Note that the cyclonic-slantwise wrapping, which is more significant along the convective band, is described herein in a volume-averaged sense due to the collective effects of deep convection (i.e., upward motion) coupled with the cyclonic flow. In reality, air parcels embedded in (meso-γ-scale) convective updrafts or downdrafts tend to move more vertically than horizontally. Thus, this concept differs from that in a typical baroclinic system in which weak, stable ascent often occurs along frontal zones.

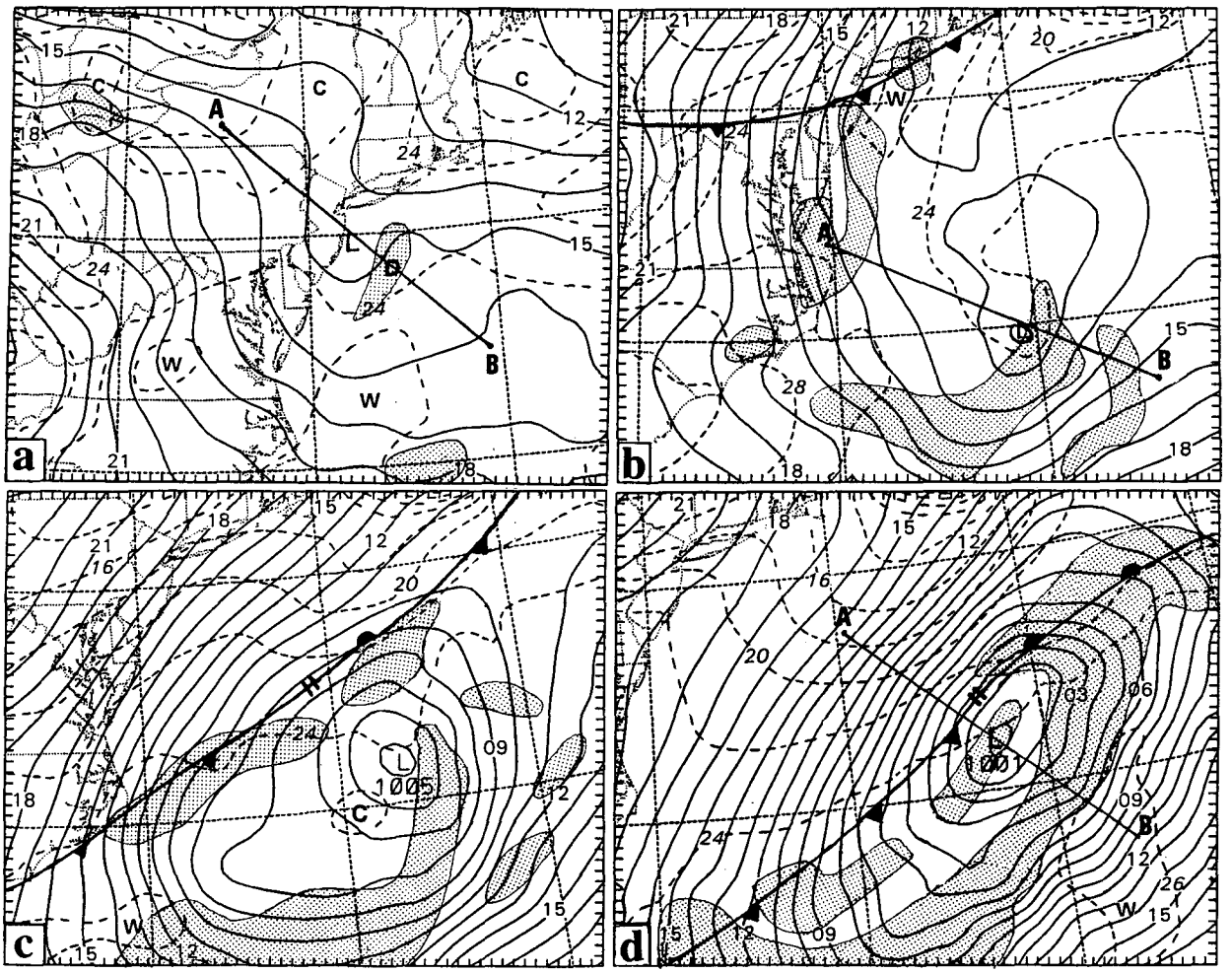

FIG. 1. Simulated sea level pressure (solid, every 1 hPa), labeled as an excess over 1000 hPa, e.g., 06—1006 hPa, and surface temperature (dashed, every 2°C) at (a) 20/12-24; (b) 22/00-60; (c) 22/12-72; and (d) 23/00-84. Lines *AB* indicate location of cross sections used in subsequent figures. Shadings denote the area of simulated deep convection. The intervals marked on the frame are mesh grids (25 km for fine mesh; similarly in the rest of figures). Letters "L," "W," and "C" denote the centers of the surface cyclone, warm and cold air, respectively.

Six hours later (i.e., at 22/06-66), the larger-scale background flow becomes better organized (Fig. 2b) as the surface cyclone deepens. The two *V*-bands are also amplifying as they are displaced cyclonically toward the cyclone center where weak flows are prevailing (cf. Figs. 1b and 2a,b). A closed wind circulation with increased curvature vorticity begins to form near the center. Of interest is that *the developing cyclone absorbs gradually and overpowers the lower-level circulation of the mesovortex* as the convective *V*-band propagates into the weak-flow region (cf. Figs. 2a–c). Vorticity budgets, as shown in Fig. 8, reveal that stretching due to convergence in the planetary boundary layer (PBL) contributes the most to the amplification of the two *V*-bands. Hence, the cyclonic vorticity is primarily generated through vortex stretching along the *V*-bands, and then advected cyclonically toward the cyclone center in a slantwise fashion, causing the intensification of the cyclone.

By 22/12-72, an organized mesovortex has formed at 950 hPa as the surface cyclone becomes well developed ahead of the large-scale cold front (cf. Figs. 1c and 2c). Over the vortex center, the relative vorticity, which was less than $0.5f$ 12 h earlier, has tripled to more than $2f$. Meanwhile, the cyclonic vorticity in the storm's northwestern quadrant has increased. Of particular importance is the development of a "comma-shaped" vorticity structure, in which the "comma" head contains mostly curvature vorticity while its tail consists of shear vorticity. This "comma" head forms as the local vorticity maximum moves into the weak-flow area (cf. Figs. 1b,c and 2b,c). These vortex features, including the associated wind, pressure and precipitation structures, are very similar to the comma vor-

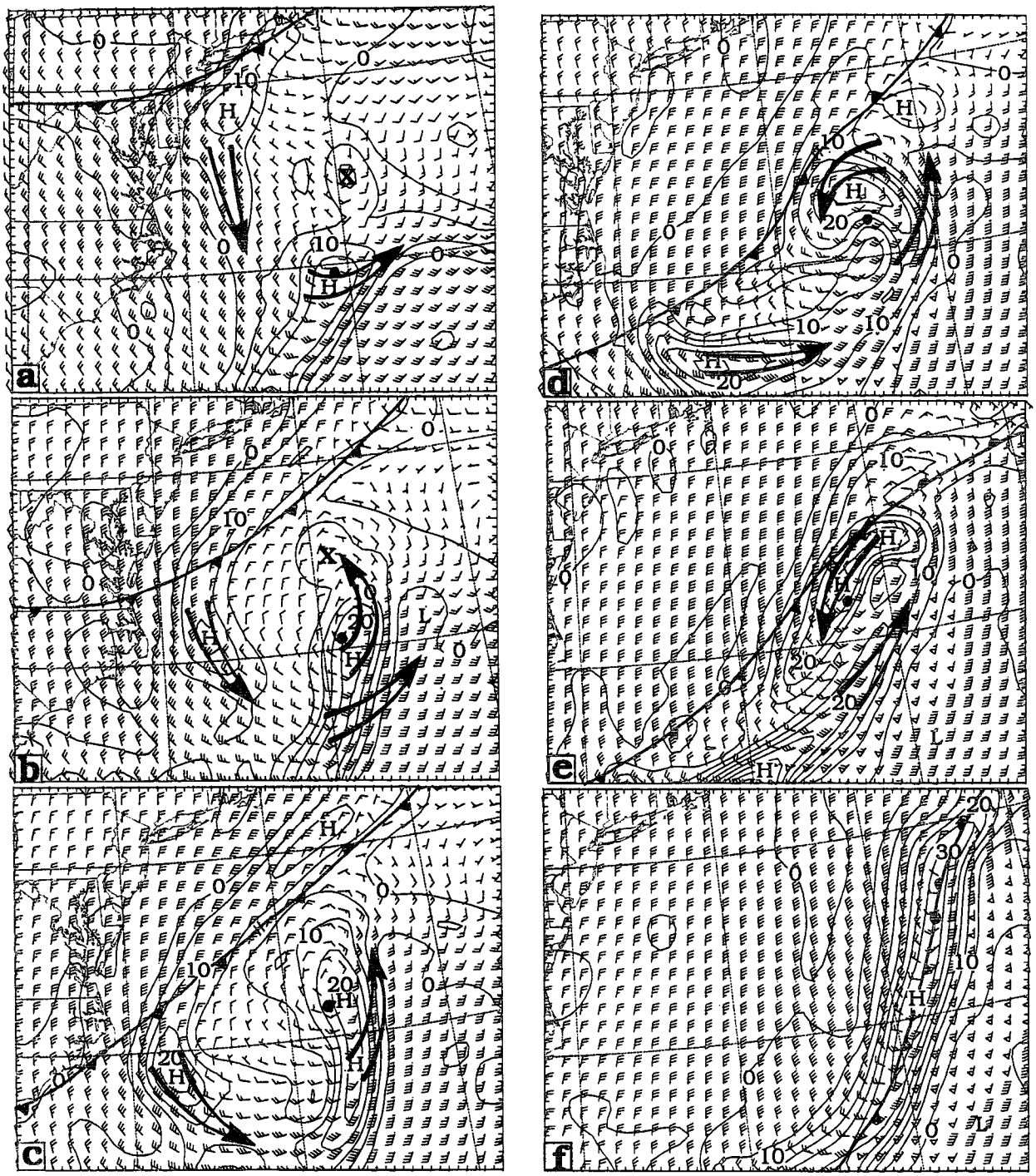

FIG. 2. Horizontal maps of vertical relative vorticity at 950 hPa at intervals of 5×10^{-5} s^{-1} superposed with horizontal winds plotted at every other grid point at (a) 22/00-60, (b) 22/06-66, (c) 22/12-72, (d) 22/18-78, (e) 23/00-84, and (f) 23/06-90. Winds plotted according to convention with each pennant, full barb, and half barb denoting 25, 5, and 2.5 m s^{-1}, respectively. Large arrows indicate the direction of propagation of the vorticity centers. Solid circle denotes the center of the surface cyclone. The surface frontal position, based on the evolution of θ_e, is given (see Part I). The symbol "X" shows the part of relative vorticity associated with the mesovortex.

tex described by Tuleya and Kurihara (1984) in their simulation of tropical cyclogenesis. Their results also show that the comma vortex forms as a consequence of the vortex stretching along a convective band and advection into the cyclone center. This suggests that the continued deep convection along the oceanic storm

is crucial in the formation of the comma vortex and the deepening of the surface cyclone (cf. Figs. 2 and 3). In other words, *the vortex/cyclone system deepens as the convectively generated shear vorticity (through stretching) is advected inward and converted to curvature vorticity* (see the appendix for more explanations), at least during the cyclone's incipient stages. The significant advective effects are understandable, when considering the relatively weak vertical motion or convergence near the cyclone center (see Figs. 4 and 5). This argument is also in agreement with the principle of angular momentum conservation in the presence of a low-level jet.

At 22/18-78, the main portion of the baroclinic V-band has moved into the convective band ahead of the cold front. It has traveled at a speed of 10–12 m s^{-1} during the previous 18 h, which is about 65% of the average wind speed at the local vorticity center (Fig. 2d). The merging of this V-band into the convective V-band leaves behind very weak cyclonic vorticity along the southwest–northeast-oriented cold front, consistent with the analysis of little wind shift across the surface front by BS81. By comparison, the major portion of the convective V-band has been wrapped around into the circulation (but not the low pressure) center with much less vorticity left in the tail of the comma vortex. As a result, an intense cyclonic circulation with strong winds develops in the vicinity of the vortex center (cf. Figs. 2a–d). Note that the wrapping-around of the two V-bands as well as the high-θ_e tongue appears to "block" the large-scale flow and distort the frontal zone. For example, the flow behind the cold front changes its direction from north-northwesterly at 60 h to near-northerly at 66 h, northeasterly at 72 h, and north-northeasterly at 78 h (see Figs. 2a–d). This blocking appears to help explain why the surface cold front slows after it moved over the ocean (but the opposite is true in the BS81 analysis, see their Fig. 21).

By 23/00-84, the cyclonic wrapping-around has advected the leading portion of the convective V-band into the northerly flow, as occurred with the 900-hPa high-θ_e tongue (cf. Fig. 13c in Part I and Fig. 2e herein). It is apparent that the wrapping-around of both the V-bands and the high-θ_e air is highly asymmetric, and it occurs slightly faster than the propagation of deep convection along the low-level jetlike current. In contrast, the baroclinic V-band has moved completely into the southwesterly flow and merged with the convective V-band, resulting in the rapid growth of cyclonic vorticity along the oceanic storm; its peak intensity has increased to over $4f$. Note that this portion of V-band coincides with the broad trough ahead of the cold front, whereas the concentrated vorticity in the northerly flow ($>3f$) corresponds to the "oval-shaped" surface isobars with its peak located slightly ahead of the surface mesolow (cf. Figs. 2e and 1d). Note also that the closed wind circulation always leads the surface mesolow (see Figs. 2a–e), indicating *the important role of the vorticity concentration in driving the propagation and intensification of the oceanic cyclone.* Of interest is that the intense vorticity concentration in the northerly flow tends to be sheared away as the frontal circulation begins to dominate the cyclone's flow structure (cf. Figs. 2d–f). In fact, the lateral dimension of the peak vorticity zone has already decreased and more curvature vorticity has been converted to shear vorticity during the previous 6 h (cf. Figs. 2d,e). This vorticity conversion can also be seen from Eq. (A1) in the appendix, in which the two terms on its right-hand side (rhs) become negative as the vorticity center is advected away from the closed circulation center (i.e., with decreasing curvatures along the frontal zone). Hence, the comma vortex begins to transform into a linear vortex band hereafter.

At the end of the 90-h integration, the cold front has merged with the surface cyclone, causing the collapse of the wrapping-around process and the development of an elongated V-band that consists mostly of shear vorticity (see Fig. 2f). It is clear that this intense cyclonic vorticity is the result of convective and baroclinic (vorticity) interaction associated with the convective band and the large-scale front over a period of 36 h. Hereafter, the large-scale baroclinic forcing begins to influence the evolution of the oceanic storm. Nonetheless, the intense south-to-southwesterly surface jet, with speeds greater than 30 m s^{-1}, is seen closely related to the development of the convective band.

To quantify the relative significance of the convective versus baroclinic forcings in generating the vorticity structures presented above, a sensitivity simulation is performed in which both the grid-scale latent heat release and the convective schemes are gradually turned off after the first 24-h integration (experiment NLH). It is obvious from Fig. 3 that the model produces a band of cyclonic (shear) vorticity associated with the low-level southwesterly jet at 22/00-60; but its magnitude is at most 40% of that along the convective V-band in the control run (cf. Figs. 2a and 3a). Since the low-level winds and horizontal shears in the vicinity of the dissipated MCSs at 20/12-24 are weak and since this V-band coincides well with the southwest–northeast elongated convergence zone offshore (cf. Figs. 19–21 in Part I and Fig. 3a herein), we may state that the stretching of planetary vorticity *during the previous 36 h* accounts for the generation of such a low-level V-band. Because of the continued weakening of the mesovortex circulation in the absence of diabatic heating, its lower-level residue vorticity could not be maintained as in the control run (cf. Figs. 2a, 3a, and 4a,b). Otherwise, stretching of the vortex's residue vorticity would also make some but secondary contribution to the V-band. After another 24-h integration, that is, at 23/00-84, the intensity of the V-band has increased slightly due to the continued stretching production (of absolute vorticity) against dissipative destruction, but with no sign of a closed circulation or

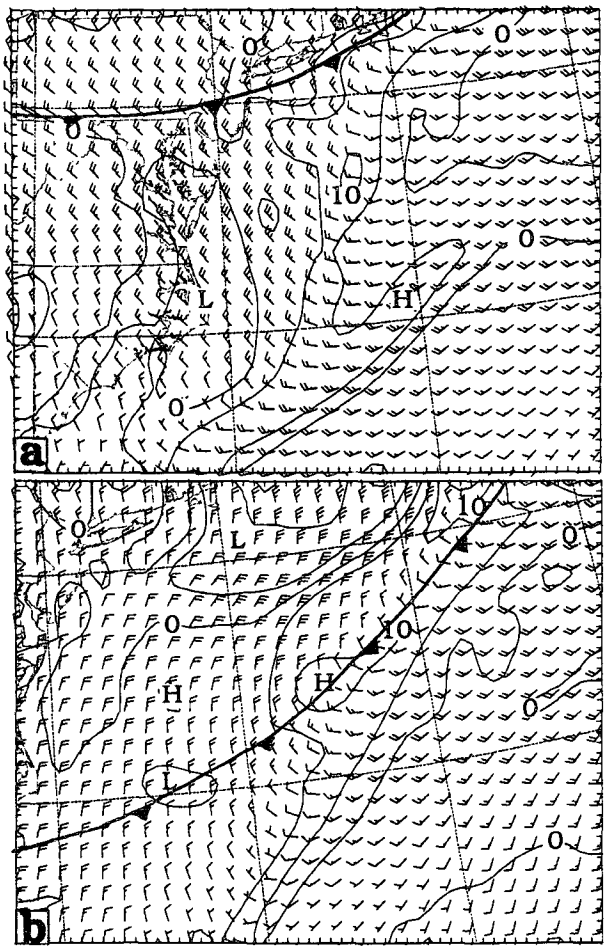

FIG. 3. As in Fig. 2 but from experiment NLH (i.e., no latent heating) at (a) 22/00-60 and (b) 23/00-84.

a comma-shaped vorticity pattern. This is consistent with the simulation of a surface frontal trough at the end of the 84-h integration (see Fig. 14 in Part I). Furthermore, the magnitude and area coverage of the V-band are much smaller than those associated with the control-simulated. All this reinforces the previous conclusion that the intense vorticity concentration near the cyclone center and their wrapping-around features are mainly a consequence of the convective development along the oceanic storm.

3. Vertical structures

To gain insight into the aforementioned low-level wrapping-around processes in relation to the midlevel mesovortex, Figs. 4a–c show vertical cross sections of relative vorticity and horizontal winds through the center of the surface mesolow at the three important life-cycle stages, that is, the dissipation of the continental MCS and the incipient and mature stages of the oceanic storm. Figures 5a–c present the corresponding height and temperature deviations as well as vertical motion. All deviations are obtained by deducting their pressure-level averages in the cross section. One can see from Figs. 4a and 5a that the continental MCSs leave behind a deep and vertically coherent mesovortex up to 450 hPa at 20/12-24. This deep circulation is associated with a deep layer of lower heights (i.e., the short-wave trough). It is apparent that this short-wave trough, with the maximum intensity occurring near 650 hPa, is characterized by a warm core (>2°C) above 650 hPa and a cold anomaly (<−2°C) below (see Fig. 5a). As shown in ZF86, Zhang et al. (1988), and Zhang (1989), these vertical thermal anomalies are produced by parameterized and grid-scale heating aloft and moist downdrafts and evaporative cooling below within the continental MCSs. Such a vertical thermal structure has been observed at the early stages of tropical cyclogenesis during TEXMEX (see Emanuel et al. 1993; Lopez et al. 1993; Bister and Emanuel 1994) and it is also of typical to continental MCSs near the end of their life cycle (BS81; Fritsch et al. 1994). *Because of the cold*

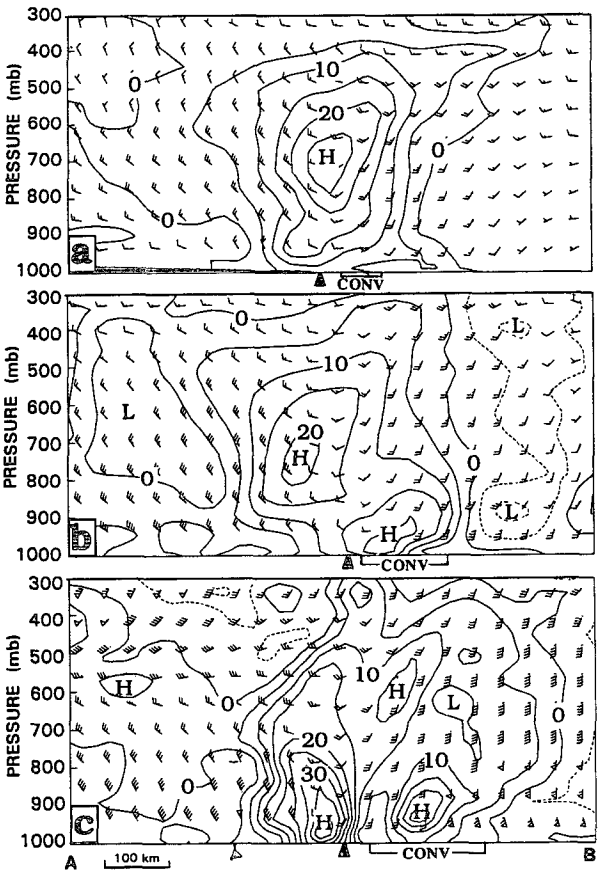

FIG. 4. Vertical cross sections of vertical relative vorticity at intervals of 5×10^{-5} s^{-1} and horizontal winds (see Fig. 2 for plotting convention) at (a) 20/12-24, (b) 22/00-60, and (c) 23/00-84, which are taken along line *AB* as given in Figs. 1a, 1b, and 1d, respectively, with a length scale of 800 km. Symbols along the abscissa show locations of the cold front, the surface cyclone center (▲) and the convective forcing region (CONV).

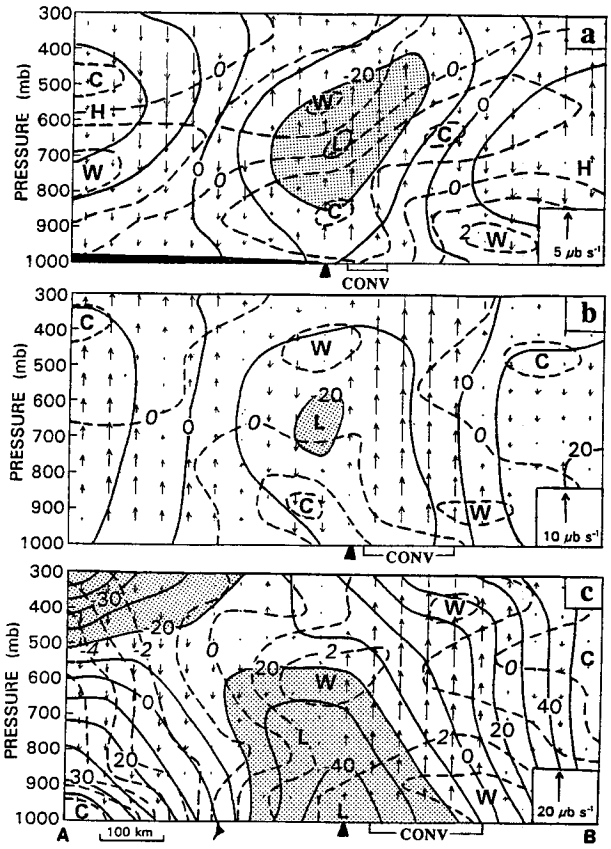

FIG. 5. As in Fig. 4 but for deviation heights (solid, every 10 m) and deviation temperature (dashed, every 1°C), superposed with vertical motion. Shadings denote negative height anomalies less than −20 m. Symbols along the abscissa give locations of the cold front, the surface cyclone center (▲) and the convective forcing region (CONV).

(warm) anomaly in the lower (upper) portion of the mesovortex, the magnitude of the short-wave trough decreases toward the surface (upward), leading to a much weaker surface pressure trough (cf. Figs. 5a and 1a), as has been noted during TEXMEX. It follows that *mesovortices tend to be better maintained at the interface between the warm anomaly above and cold pool below.* Such a vertical thermal/vorticity juxtaposition could also be expected from balanced flow considerations. It should be pointed out that these convectively generated vortex structures differ markedly from those in cold-core extratropical cyclones, which exhibit considerable vertical tilt in their developing stages.

It is important to notice the distribution of vertical motion with respect to the vortex circulation, although it is very weak everywhere at this stage. Specifically, the mesovortex is generally accompanied by upward motion ahead, though influenced by the dissipated MCS at this hour, and descending motion behind (Fig. 5a). This upward motion, which is more evident later in the lower levels, persists in the southwesterly flow of the vortex circulation even in the absence of diabatic heating (see Figs. 19–21 in Part I). This forcing provides a favorable condition for the later initiation and organization of deep convection (e.g., see Fig. 5b). It is also important to notice that the vortex is embedded in an environment with very weak vertical shear except in the lowest 100 hPa (Figs. 4a,b); the strongest flow (<15 m s^{-1}) occurs near 700 hPa behind the vortex. As discussed in Part I, such an environment is favorable for the maintenance of a midlevel mesovortex. It is apparent that Raymond and Jiang's (1990) argument[3] for long-lived MCSs cannot be used here to explain the redevelopment and maintenance of the MCS owing to the presence of weak vertical shear.

At 22/00-60, although the magnitude of the midlevel mesovortex has decreased by about 20% compared to that 36 h earlier, little change has taken place with its vertical structure, except in the lowest 100 hPa where the cyclonic vorticity near the center has decreased notably (see Fig. 4b). It should be noted, however, that these changes in intensity are mainly caused by the vertical cross section that is taken through the center of the surface mesolow rather than of the mesovortex (see their different tracks given in Fig. 1 of Part I). This result is remarkable, since the long-lived vortex circulation helps explain why certain MCSs, like those analyzed by Wetzel et al. (1983) and Fritsch et al. (1994), could sustain or undergo multiple developments when organized larger-scale energy supplies are available. Of particular relevance at this stage is the formation of a pronounced low-level V-band at the southeast periphery of the midlevel vortex/trough, a feature that has been observed during TEXMEX (Emanuel et al. 1993). As previously mentioned, this V-band is convectively generated along the oceanic storm (as marked by "CONV" in Figs. 4, 5, and 7), and it is this V-band that wraps around to contribute to the subsequent amplification of the surface cyclone. It is worthwhile noting that this convectively generated vorticity profile differs considerably from that which occurred with its continental counterpart. That is, the continental vortex occupies a deep layer in the vertical with its maximum intensity occurring between 800 and 700 hPa (see ZF87 and Fig. 4a), whereas the oceanic V-band is only confined in the lowest 200 hPa with its peak near 950 hPa. Since vortex stretching is the primary vorticity forcing in both cases, this difference appears to reflect different environments in which they are generated. Specifically, the continental vortex develops in the trailing stratiform region of the MCC at the base of the midlevel short-wave trough with considerable preexisting curvature vorticity, whereas the oceanic V-band forms along the convective band along the *low-level southwesterly jet,* thus having maximum

[3] In their study, Raymond and Jiang (1990) discussed how the diabatically generated positive potential vorticity anomaly in the lower troposphere interacts with a sheared environment in the maintenance of a long-lived MCS.

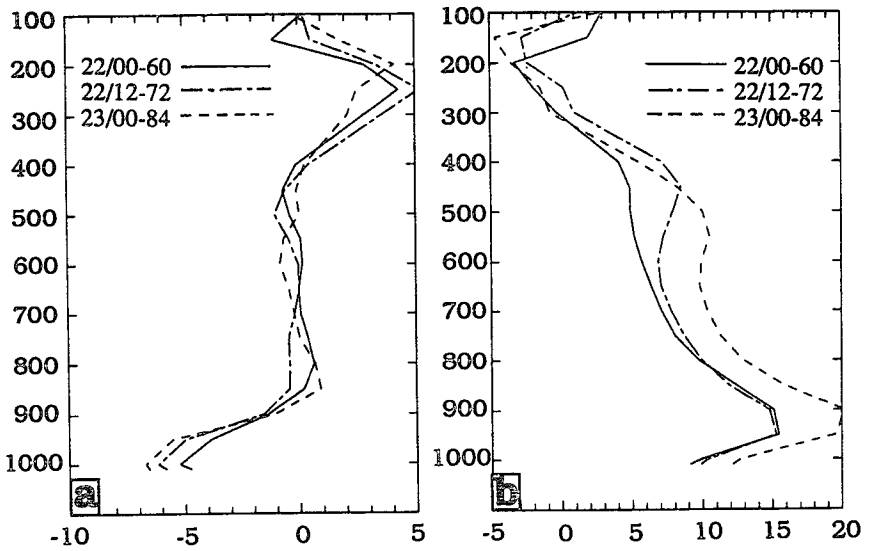

FIG. 6. Vertical composite profiles of (a) divergence (10^{-5} s^{-1}) and (b) relative vorticity (10^{-5} s^{-1}) that are obtained by averaging them along the vorticity axis of the convective band with a lateral scale of 150 km at 22/00-60 (solid), 22/12-72 (dot–dashed), and 23/00-84 (dashed).

shear vorticity close to the ocean surface. Furthermore, the maximum convergence, determining the cyclonic vorticity production, occurs at a higher level in the continental MCC (often near the melting level, see Houze 1989) than that along the present convective band (cf. Figs. 9, 10 in ZF87 and Figs. 5b, 6 herein). In the oceanic case, more intense convergence or vortex stretching develops in the lowest 100 hPa and decreases abruptly upward (Fig. 6a), which is consistent with the low-level concentration of cyclonic vorticity (Fig. 6b). Such a vertical profile appears to be attributable to the development of weaker convectively generated downdrafts and the presence of weaker frictional dissipation in the maritime boundary layer.

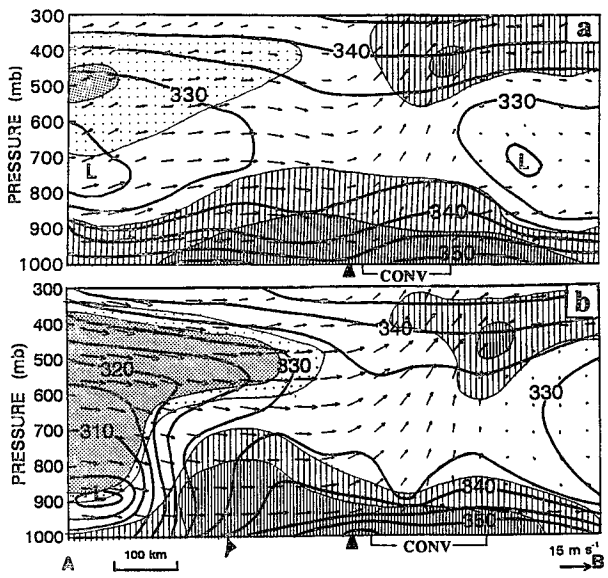

FIG. 7. As in Figs. 4b,c but for equivalent potential temperature θ_e at intervals of 5 K, superposed with along-plane flow vectors. Only the scale of the horizontal speed is given. Wide (narrow) hatching denotes areas with RH > 70% (80%), whereas coarse (dense) shading denotes areas with RH < 40% (30%). Symbols along the abscissa give locations of the cold front, the surface cyclone center (▲), and the convective forcing region (CONV).

At this incipient stage of the surface redevelopment, height deviations also exhibit somewhat different vertical structures from those that occurred 36 h earlier. Specifically, there is an increase in height gradients in the lower levels (i.e., below 850 hPa) but a decrease of the gradients aloft ahead of the vortex (Fig. 5b). This is in agreement with the tightening of the surface isobars (cf. Figs. 1a,b) and the development of the low-level southwesterly jet and the convective V-band (see Figs. 2a,b and 4b). Similar changes in height gradients also take place to the rear of the system. Even though the vertical cross section is not taken through the vortex center, we still can see that the midlevel short-wave trough is again hydrostatically maintained by the warm anomaly aloft and the cold anomaly below (Fig. 5b). This suggests that this thermal anomaly couplet has propagated in pace with the mesovortex. In other words, *this vertical thermal couplet should be considered as a basic element of the vortex/trough system* in the presence of little vertical shear. Moreover, the maintenance of the low-level cold anomaly in the present case does not require further evaporation of rainwater from the MCS as hypothesized by Emanuel et al. (1993).

A vertical cross section of relative humidity and equivalent potential temperature θ_e, given in Fig. 7a,

shows the presence of relatively higher-θ_e and moister columns along the convective band (CONV) in the southwesterly portion of the vortex flow. This mid- to upper-level moistening is achieved by the parameterized detrainment in the Kain and Fritsch (1990, 1994; hereafter KF) convective scheme and mesoscale ascent, whereas at the lower levels, a θ_e ridge is produced along the convective band as a result of the upward transfer of surface fluxes and vertical advection. It has been illustrated in Part I that this low-level θ_e anomaly tends to wrap around in a slantwise fashion into the cyclone center, causing conditional instability in the vicinity of the convective band. Of significance is that the mesovortex has always been accompanied by a midlevel high-θ_e anomaly, just like its pertinent cyclonic vorticity structure (cf. Fig. 11 in ZF87 and Figs. 5a,b herein). As discussed by ZF87, this is due partly to the inertial stability of the vortex, which produces resistance to radial transport of energy, and partly to the weak-sheared environment, which slows down the transport of energy away from the vortex columns. The two factors are essentially responsible for the maintenance of the vortex circulations in a vertically coherent manner.

At the cyclone's mature stage, that is, 23/00-84, both the height gradients and horizontal winds have experienced considerable increases, especially at lower levels (Figs. 4c and 5c). Likewise, stronger mesoscale ascent ($\sim$20 μb s^{-1}) and cyclonic vorticity have developed along the convective band. Vertical composite divergence and vorticity profiles also exhibit the continued amplification (see Figs. 6a,b), but with more significant changes taking place in the lowest 200 hPa. Of particular interest is the development of a concentrated V-band up to 700 hPa in the vicinity of the cyclone center, with its maximum magnitude exceeding 40×10^{-5} s^{-1}. The lower-level concentration of intense cyclonic vorticity, like that shown in Fig. 6b, is also a typical feature of tropical cyclones (Frank 1977; Davidson et al. 1990). However, the precise dynamic mechanism responsible for such a vorticity concentration still remains elusive. Based on their Doppler radar analysis and Davidson et al.'s (1990) dataset, Mapes and Houze (1993) suggested that this intense vorticity could be generated as the midlevel mesovortex descends to the surface and then amplifies in the presence of intensifying low-level inflows. We have shown in section 2 that this low-level intense vorticity forms at the southern periphery of the midlevel mesovortex as a consequence of the slantwise wrapping around of shear vorticity that is generated along the convective band, and then converted to curvature vorticity. This discrepancy is likely due to their datasets that are either too coarse to resolve the convectively generated vorticity structures along rainbands using the Australian tropical analysis in Davidson et al. (1990; 1.25° latitude–longitude grid) or too limited to cover both the vortex and rainband circulations using airborne Doppler radar observations in Mapes and Houze (1993). Thus, our result clearly suggests that obtaining a reasonable description of individual rainbands and their collective effects on tropical cyclogenesis with high-resolution observations or numerical simulations is instrumental in understanding different processes that are responsible for oceanic or tropical cyclogenesis.

The relationship between the low-level vorticity amplification and the midlevel mesovortex can be inferred from Figs. 4b,c and 5b,c. It is seen that ascending motion always dominates the southwesterly portion of the vortex circulation where the convective V-band intensifies, whereas weak vertical motion occurs elsewhere. Thus, the mesovortex makes little direct contribution, that is, through vertical advection, to the generation of the intense vorticity at 950 hPa. Moreover, the low- and midlevel vorticity anomalies remain as two separate entities until the surface cyclone enters the mature stage and overpowers completely the mesovortex circulation (Figs. 4b,c). Of course, it by no means indicates that the mesovortex has little impact on the development of the vorticity band. In fact, the vortex circulation provides a favorable condition for the deepening of the cyclone, at least, *the necessary cyclonic vorticity to stretch in the presence of convergence in the PBL.* This could be seen from Figs. 2–5, which shows that the convective V-band amplifies within a broad cyclonic circulation. The more important role of the mesovortex has been shown in Part I to assist the initiation and organization of deep convection along the oceanic storm. In this respect, the oceanic cyclogenesis should be regarded as induced by the mesovortex/MCS system through the stretching of its residue cyclonic vorticity and the organization of deep convection in the right environments (e.g., ahead of the trough axis, the land–ocean contrasts, the warm Gulf Stream water, and tropical energy supply). Once it is established, the cyclone tends to overpower the vortex circulation, at least in the lower troposphere. On the other hand, deep convection along the oceanic storm helps intensify the midlevel mesovortex (see Figs. 17b,c in Part I and Fig. 6b herein) mainly through vortex stretching in the ascending flow, as will be seen in the next section. Without it, experiment NLH shows the continued weakening of the vortex under the influence of numerical diffusion and (weak) larger-scale deformation (e.g., see Fig. 3).

Similar to the deep vorticity concentration, a deep θ_e ridge (up to 700 hPa) is generated to the northwest of the cyclone, that is, in the cyclonic northerly flow (cf. Figs. 13c in Part I and 7b herein). It is apparent that this θ_e ridge results from the slantwise wrapping-around of the high-θ_e air generated along the convective band, as shown in Part I, since θ_e is a conserved variable in an inviscid, pseudoadiabatic flow and since little upward motion occurs in the cyclonic northerly flow. (The θ_e trough between the two ridges corresponds to a lower-θ_e slot embraced by the high-θ_e tongue in Fig. 13c of Part I.) In addition, the wrapping-around process produces a deep "wall-like" θ_e structure behind the

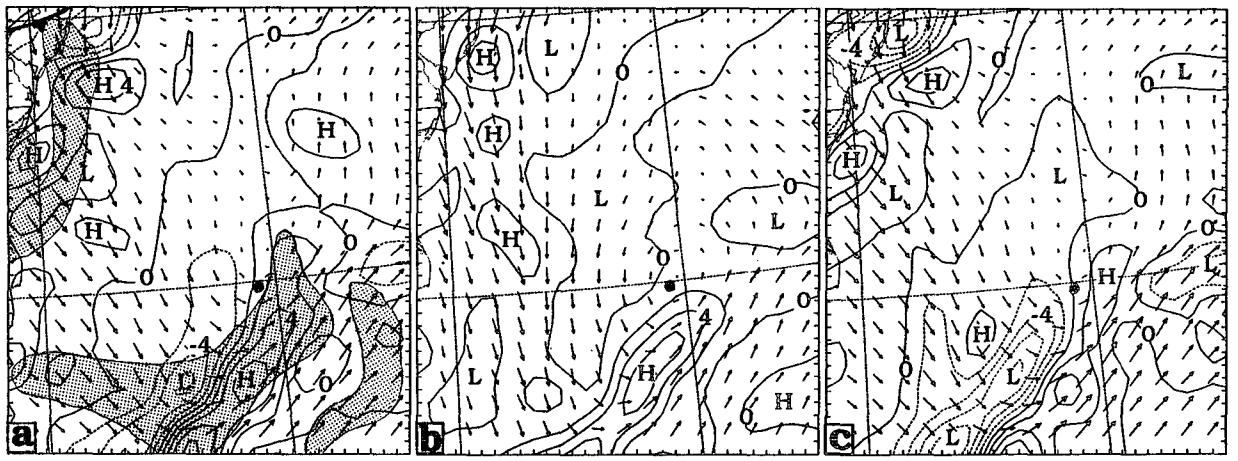

FIG. 8. Horizontal maps of the relative vorticity budget at intervals of 2×10^{-5} s^{-1} h^{-1} at 950 hPa from 60-h simulation (i.e., 22/00-60): (a) local vorticity tendency ($\partial\zeta/\partial t$); (b) vortex stretching ($-\eta\nabla\cdot\mathbf{V}$); and (c) horizontal advection ($-\mathbf{V}\cdot\nabla\eta$). Superposed are wind vectors at 950 hPa plotted at every other point (1 grid length represents 14 m s^{-1}) except for (b) in which system-relative winds are plotted. Solid (dashed) lines are positive (negative) tendencies. Solid circle denotes the surface cyclone center. The surface frontal position and the convective distribution, as shaded, are given in (a).

cold front, which is again an indication of the blocking effect of the cyclone on the movement of the frontal system. For a similar reason, the low-level cyclonic flow transports ambient warmer air into the vicinity of the cyclone, thereby *eliminating the cold anomaly in the lower portion of the troposphere* (cf. Figs. 5a–c and 7b); see section 5 for the depiction of horizontal thermal advection. (A wall-like deviation thermal profile is also evident to the rear of the system.) As a result, the surface cyclone is now situated beneath a deep column of relatively warmer air, causing the greatest pressure drop *at the surface* (see Fig. 5c). Such a transformation from the cold to warm anomalies in the lower troposphere has been observed at the cyclogenesis stage during TEXMEX (see Emanuel et al. 1993). In the present case, the transformation takes 24 h as the lower troposphere is gradually warmed and the mid-level mesolow becomes less distinct in shape. It is evident that the advancing cold front, even though it is accompanied by larger-scale descent, does not make notable contributions to the thermodynamic transformation as well as to the cyclogenesis, since the aforementioned process occurs in a near-barotropic environment after 22/00-60 when the surface front is more than 600 km away from the cyclone center. Likewise, the upper-level baroclinic trough provides little vorticity forcing to the surface cyclogenesis (cf. Fig. 4c herein and Fig. 17c in Part I). The large-scale flow, including the baroclinic trough/cold front and a subtropical high, appears to play a role in steering the propagation of the oceanic storm/cyclone system, as discussed in Part I. It is also evident that the cyclone will continue to deepen as long as more high-θ_e air can be transported into the system and more deep convection develops.

4. Vorticity budgets

After seeing in the preceding two sections the kinematic structures and evolution of cyclonic vorticity associated with the oceanic cyclone/storm system, it is desirable to examine quantitatively what dynamic processes are responsible for the spinup of the cyclone's vorticity. This is done in this section by computing the three-dimensional vorticity budget using the dynamically consistent model dataset. The vorticity equation in isobaric coordinates is

$$\frac{\partial\zeta}{\partial t} = -\mathbf{V}\cdot\nabla\eta - \omega\frac{\partial\zeta}{\partial p} - \eta\nabla\cdot\mathbf{V} - \mathbf{k}\cdot\left(\frac{\partial\mathbf{V}}{\partial p}\times\nabla\omega\right) + \mathbf{k}\cdot\left(\nabla\times\frac{\partial\mathbf{F}}{\partial t}\right), \quad (1)$$

where ζ is the vertical component of relative vorticity, $\partial/\partial t$ is the local tendency, $\mathbf{V}$ is the horizontal wind vector, η is the absolute vorticity, $\omega = dp/dt$, and $\mathbf{F}$ denotes the effects of boundary layer friction and numerical diffusion on horizontal momentum. The intensity changes of a cyclone can be described by its vorticity changes that are determined by the terms on the rhs of Eq. (1). They are, respectively, the horizontal advection of absolute vorticity, the vertical vorticity advection, the generation of vorticity through vertical vortex stretching, the generation of vorticity through tilting horizontally oriented vorticity into the vertical by nonuniform vertical motion, and the frictional effects due to numerical diffusion and the boundary layer flux divergence. The last three terms represent the sources and sinks of relative vorticity. All terms, including the vorticity tendency, are then computed using the instantaneous model output of all the terms in the

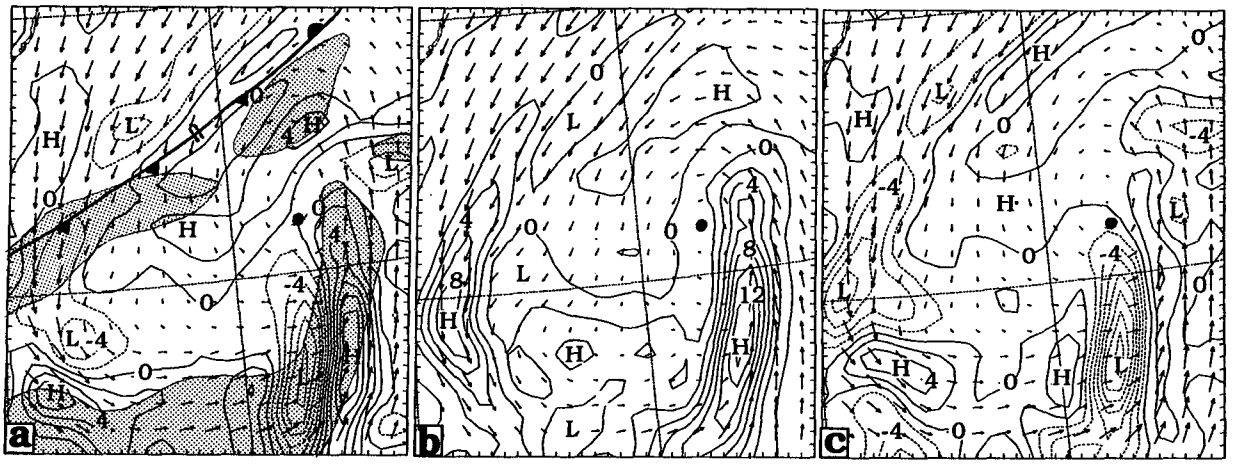

FIG. 9. As in Fig. 8 but for 22/12-72, superposed with wind vectors at 950 hPa plotted at every other point (1 grid length represents 16 m s^{-1}) except for (b) in which system-relative winds are plotted.

momentum equations. Thus, little residue will appear in the present budget calculations after excluding the effect of numerical diffusion.

Figure 8 shows the contributions of stretching and horizontal advection to the local vorticity tendencies at 950 hPa at 22/00-60 over a subdomain that is smaller than that used in Figs. 1–3. The contributions due to other terms in Eq. (1) will be presented for 23/00-84, since they are extremely small at earlier development stages. Note that after subtracting the system's translation, a closed cyclonic circulation emerges, which coincides with the first appearance of a closed isobar at this time (cf. Figs. 1b and 8b). One can see that vortex stretching exhibits marked cyclonic production along the convective band where convectively induced convergence and vorticity are maximized (cf. Figs. 2a and 8b). There is also a center of moderate cyclonic stretching tendency associated with the baroclinic V-band. In contrast, the effect of horizontal advection[4] depends on the magnitudes of cross-vorticity contour flow and vorticity gradients along the cyclonic flow. Thus, the horizontal advection always shows a couplet of cyclonic–anticyclonic contributions (cyclonic ahead of and anticyclonic behind the local absolute vorticity maximum along the current). Since the flow is skewed more along the V-bands, the cyclonic vorticity advection is much smaller in magnitude than its anticyclonic component behind except at their leading edges. The net result is that a marked cyclonic production occurs along the convective band mainly due to vortex stretching and a cyclonic reduction behind it as a result of the displacement of the V-bands (Fig. 8a). Of importance to note is the net vorticity increase at the leading edge of the convective V-band, which is consistent with the subsequent formation of a comma head over the region (cf. Figs. 2a–c and 8a). This net vorticity increase is seen to result primarily from the northeastward advection of cyclonic vorticity along the convective V-band (cf. Figs. 8a,c and 2a–c). Some minor discrepancies exist outside the convective region (Fig. 8a), which are attributable to the vertical transport of cyclonic vorticity (not shown).

At 22/12-72, the formation of the comma vortex causes significant alterations in the cyclonic flow (cf. Figs. 1b,c and 2a–c). Specifically, the weak-flow air mass has been wrapped around to the wake of the convective band and the flow directions have changed from southwesterly to near-southerly along the band and from northwesterly to westerly behind it (cf. Figs. 8a and 9a). This convergent inflow tends to shrink the lateral dimension of the convective V-band (Fig. 9c) and advect its associated vorticity vertically. By comparison, the stretching contribution is always robust as the cyclone deepens; its magnitude almost doubles during the previous 12 h along both the convective and baroclinic V-bands (Fig. 9b). As before, the net effect is to increase cyclonic vorticity along the V-bands and decrease it behind (Fig. 9a). It is of interest that weak vorticity or little vorticity generation occurs along the west–east-oriented trailing portion of the oceanic storm in spite of the widespread convective development (Figs. 8a and 9a). This is because this trailing convective portion is initiated at the outer edge of the anticyclonic flow associated with a subtropical high (see Fig. 2), which is an unfavorable region for cyclonic amplification.

Figure 10 presents contributions from all rhs terms in Eq. (1) to the net vorticity tendencies at 23/00-84. Again, the net vorticity changes are dominated by cyclonic production along the convective band through

[4] Note that the north–south advection of planetary vorticity, that is, βv, accounts for less than 2.5% of the local vorticity changes associated with the baroclinic and convective V-bands, where $\beta \approx 1.8 \times 10^{-11}$ m^{-1} s^{-1}.

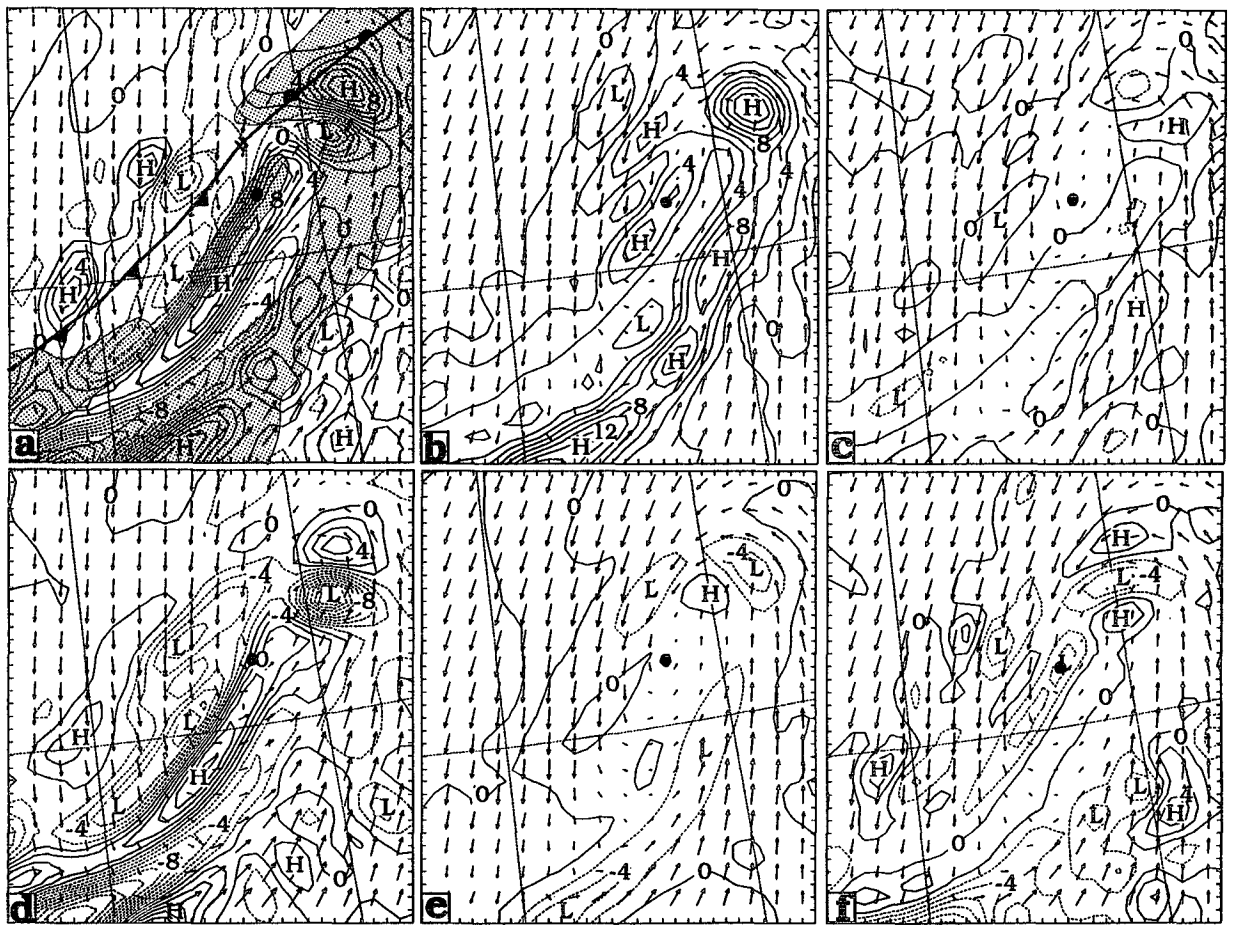

FIG. 10. As in Fig. 8 but for 23/00-84: (a) local vorticity tendency ($\partial\zeta/\partial t$); (b) vortex stretching ($-\eta\nabla\cdot\mathbf{V}$); (c) tilting of horizontal vorticity ($-\mathbf{k}\cdot\partial\mathbf{V}/\partial p\times\nabla\omega$); (d) horizontal advection ($-\mathbf{V}\cdot\nabla\eta$); (e) vertical advection ($-\omega\partial\zeta/\partial p$); and (f) frictional effects ($-\mathbf{k}\cdot\nabla\times\partial\mathbf{F}/\partial t$). Superposed are wind vectors at 950 hPa plotted at every other point (1 grid length represents 20 m s^{-1}) except for (b), (c), (e), and (f) in which system-relative winds are plotted.

vortex stretching (cf. Figs. 10a,b), and by cyclonic depletion through horizontal advection except over the leading portion of the V-band where the large cyclonic vorticity tendency is mainly associated with vorticity advection by northerly winds (cf. Figs. 2e and 10d). It should be noted that while the stretching production determines the amplification of cyclonic vorticity, the horizontal advection plays a role in transporting the necessary cyclonic vorticity to the leading portion or ahead of the V-bands for vortex stretching in the presence of intense convergence, thereby causing the wrapping-around of cyclonic vorticity. This advection–stretching interplay appears to help explain why the peak cyclonic vorticity always tends to occur at the leading edge of the V-bands (see Figs. 2a–d). Without the horizontal vorticity advection, stretching of the planetary vorticity by convectively induced convergence would be too slow a process to account for the rapid vorticity amplification, like that which occurred in the trailing portion of the oceanic storm.

As compared to the stretching contribution, the vorticity production through the tilting of horizontal vorticity is small and less organized (cf. Figs. 10b,c), due to the presence of weak vertical motion coupled with weak vertical shear along the convective band (Figs. 4 and 5). The tilting production at 950 hPa is even smaller in magnitude than the frictional destruction of cyclonic vorticity associated with downward momentum fluxes; but they are opposite in sign (cf. Figs. 10c, f). Above 950 hPa, the tilting contribution becomes anticyclonic because of the negative vertical shear, whereas toward the surface the frictional damping increases (not shown). This pronounced frictional damping has also been noted by Tuleya and Kurihara (1984; see their Fig. 11) in their tropical cyclogenesis study. The effect of upward transport over the convective regions is to reduce the cyclonic vorticity at 950 hPa and increase it above, as the system's cyclonic circulation is maximized at the level (Fig. 10e). Obviously, this leads to the increased depth of the convec-

tive V-band as it is wrapped around into the cyclonic northerly flow in a slantwise fashion (see Fig. 4c), as previously discussed. In summary, we may state that the convective V-band, shown in Figs. 2a–f, results initially from the stretching of planetary vorticity plus residue vorticity of the mesovortex, whereas the sustained vorticity growth near the cyclone center occurs as the cyclonic vorticity generated along the V-band is advected into the cyclone center and enhanced further through the stretching of absolute vorticity.

To help understand further the vertical structures of vorticity changes in relation to the midlevel vortex discussed in section 3, we present in Fig. 11 vertical cross sections of the two major vorticity contributors, that is, stretching production and horizontal advection, to the local vorticity changes at 23/00-84. Apparently, the intense vortex stretching occurs only in the lowest 100 hPa with its maximum production near 950 hPa, where both the absolute vorticity and convergence are peaked (cf. Figs. 11b, 6, and 4c). Higher up, the stretching makes cyclonic, though weak, contribution to the slow intensification of the midlevel mesovortex in the presence of relatively weak convergence associated with convectively generated secondary circulations (see Figs. 6 and 11b). The vorticity advection couplets due to the displacement of vorticity centers are also evident in deep layers. Again, the local cyclonic vorticity tendency near the cyclone center, especially above 950 hPa, results primarily from the horizontal advection of cyclonic vorticity from the convective V-band where it is generated (cf. Figs. 1d and 11a,b). This advective effect can be further seen from weak vertical motion and weak convergence in the PBL near the cyclone center (cf. Figs. 4b,c and 11b), since they indicate that both vortex stretching and tilting of horizontal vorticity are negligible over the region. At 23/00-84, however, the (narrow and shallow) stretching contribution near the center happens to be notable because of the development of a weak convective line ahead of the surface front (cf. Figs. 1d, 10b, and 11b).

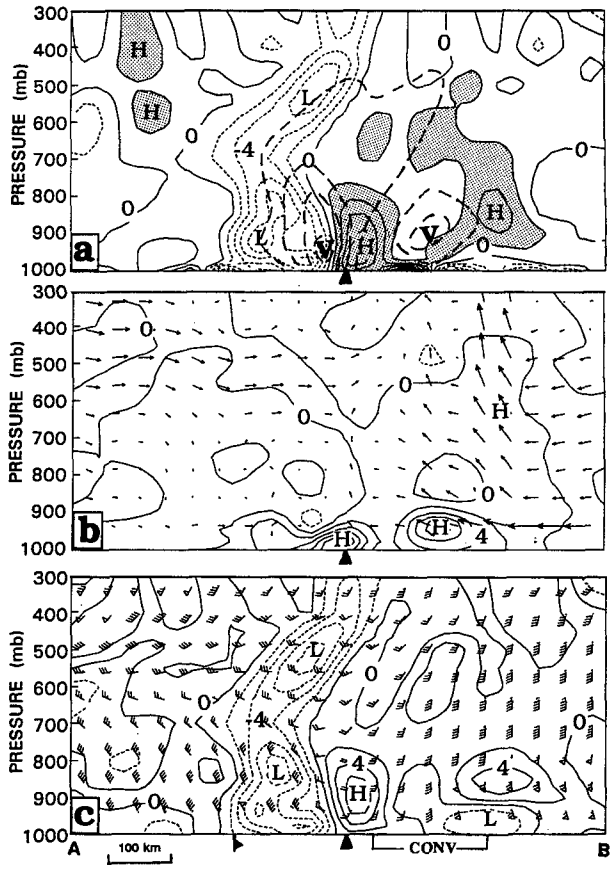

FIG. 11. As in Fig. 4c but for the relative vorticity budget at intervals of 2×10^{-5} s^{-1} h^{-1}: (a) local vorticity tendency ($\partial\zeta/\partial t$, the growth rates larger than 2×10^{-5} s^{-1} h^{-1} are shaded), superposed with cyclonic vorticity (long-dashed, every 10^{-4} s^{-1}) with the centers denoted by "V," (b) vortex stretching ($-\eta\nabla\cdot\mathbf{V}$), superposed with secondary circulation vectors that are constructed from along-plane flow perturbations (i.e., after deducting a mean flow of 8 m s^{-1}) and vertical motion; and (c) horizontal advection ($-\mathbf{V}\cdot\nabla\eta$), superposed with horizontal winds. Solid (dashed) lines are positive (negative) tendencies. Symbols along the abscissa give locations of the cold front, the surface cyclone center (▲) and the convective forcing region (CONV).

5. Thermodynamic budgets

In this section, potential temperature θ and equivalent potential temperature θ_e budgets are presented to help gain insight into the thermodynamic processes responsible for the transformation of a low-level cold pool to a warm-cored structure and the wrapping-around of high-θ_e air during the cyclogenesis stages. The prognostic θ equation in isobaric coordinates can be written as

$$\frac{\partial\theta}{\partial t} = -\mathbf{V}\cdot\nabla\theta - \omega\frac{\partial\theta}{\partial p} + \left.\frac{\partial\theta}{\partial t}\right|_{\text{PBL}} + \left.\frac{\partial\theta}{\partial t}\right|_{\text{CON}} + \left.\frac{\partial\theta}{\partial t}\right|_{\text{COND}} + \left.\frac{\partial\theta}{\partial t}\right|_{\text{DIF}}. \quad (2)$$

Terms on the rhs of (2) are, respectively, the horizontal advection, vertical advection, the contributions due to the PBL, parameterized convection, grid-scale condensation plus cloud–radiation interaction, and all numerical diffusive processes. The last four terms represent the sources and sinks of thermodynamic energy, since θ is a conserved variable in an otherwise inviscid, adiabatic flow.

For the convenience of computing the θ_e budget from the temperature and water vapor tendencies, we use the following linear form of θ_e expression:

$$\theta_e \approx \theta + \frac{L\pi}{c_p} q_v, \quad (3)$$

and

$$\pi = \left(\frac{1000\text{ hPa}}{p}\right)^{R/c_p}, \quad (4)$$

where q_v is specific humidity and all the other symbols assume their usual meteorological meaning. The prognostic equation for θ_e can be written simply by replacing θ in Eq. (2) with θ_e. Like the vorticity budget, all the terms are then calculated using the instantaneous model output of corresponding terms in the temperature and specific humidity tendency equations (see Anthes et al. 1987). Again, there will be little residue involved in the θ and θ_e budget calculations after excluding the effect of numerical diffusion (i.e., $\partial\theta/\partial t)_{\text{DIF}}$.

To facilitate the subsequent discussion of the θ and θ_e budgets, Fig. 12 shows the evolution of the thermal and height structures at 900 hPa where the negative thermal deviation is peaked prior to the cyclogenesis (see Figs. 5a,b). It is seen that a cold pool, left behind by the previous MCS, has propagated in pace with the trough/vortex system until 22/00-60. There are a warm tongue in conjunction with the cyclonic flow from the southeastern states eastward around the cold pool, a cold air mass to the southeast, and the rapidly propagating cold front from the northwest. It is of particular importance that the oceanic mesolow, as marked by "L_c," is initiated at the southeast periphery of rather than near the center of the cold pool (also see Figs. 2a–c), as also mentioned in Part I. This mesolow corresponds closely to the development of a cyclonic vorticity center along the convective V-band with little evidence of a warm anomaly in the lower troposphere (cf. Figs. 2a, 5b and 12a), suggesting that *it is driven by the convectively generated vorticity field.* Because of this nonconcentric phase difference between the vortex and the new mesolow, the intensifying cyclonic flow, which overpowers quickly the vortex circulation in the lower levels, tends to destroy the cold-pool structure by advecting the associated cold air in its northerly flow into the convective band and the ambient warmer air into the system—a reflection of the cyclone–convection interaction (see Fig. 12b). By 23/00-84, the cold pool has been completely absorbed by or circulated into the convective storm, causing a slight cooling of the warm tongue (cf. Figs. 12b,c). As a result, the isotherms become linearly distributed ahead of the cold front, which are in significant contrast to the original circular pattern of the cold pool (cf. Figs. 12a,c). It is apparent that the thermodynamic transformation is primarily driven by the intensifying cyclonic circulation, namely, the organized vorticity field. Note that the convective band is always distributed along the warm (or high-θ_e) tongue (cf. Figs. 1 and 12), and the cyclone is now seen to draw warmer air from the east to northeast into the system. Evidently, the thermodynamic transformation in the present case, at least above 950 hPa, differs from the hypothesis of Emanuel et al. (1993) that the cold pool is mainly heated through the upward transfer of surface heat and moisture fluxes over warm ocean.

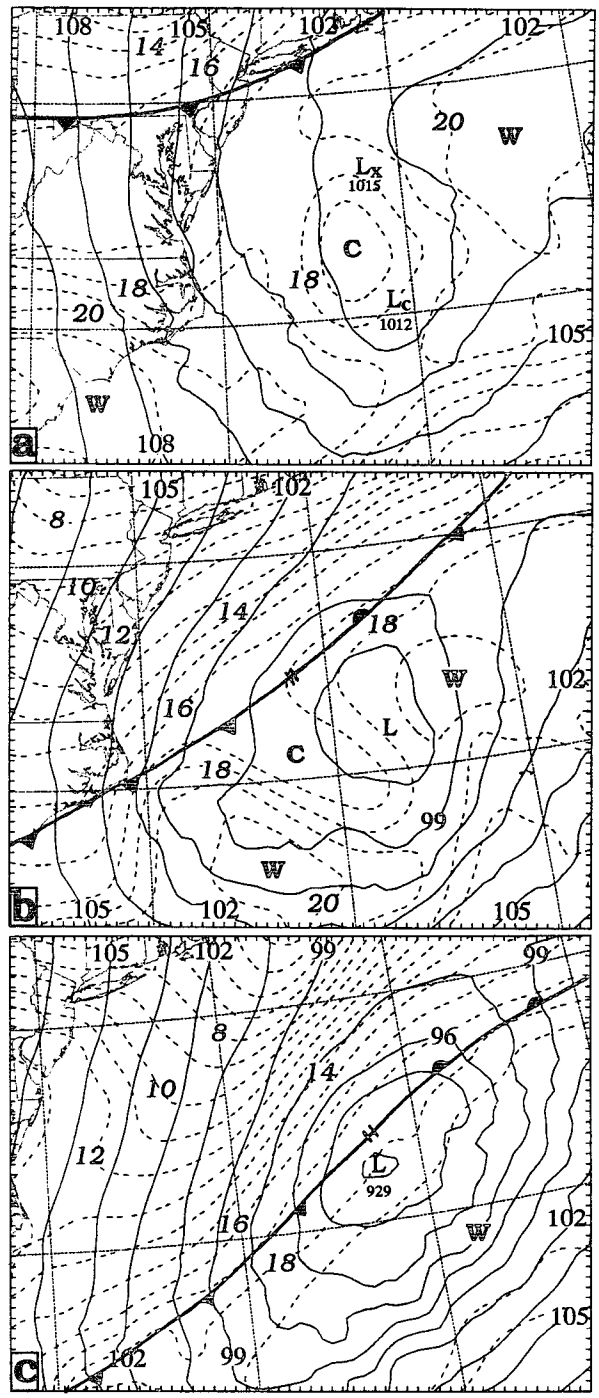

FIG. 12. Simulated geopotential height (solid) at intervals of 1.5 dam and temperature (dashed) at intervals of 1°C at 900 hPa at (a) 22/00-60, (b) 22/12-72, and (c) 23/00-84. Letters "L_x" and "L_c" in (a) denote the minimum central heights at 900 hPa associated with the vortex/trough and the new mesolow, respectively.

Some selected maps of the θ budget during the thermodynamic transition period, that is, at 22/12-72, are presented in Fig. 13, which does show the evidence of cold advection into the convective storm in the cyclonic northerly flow and warm advection into the cyclone system from the northeast of the cyclone (cf. Figs.

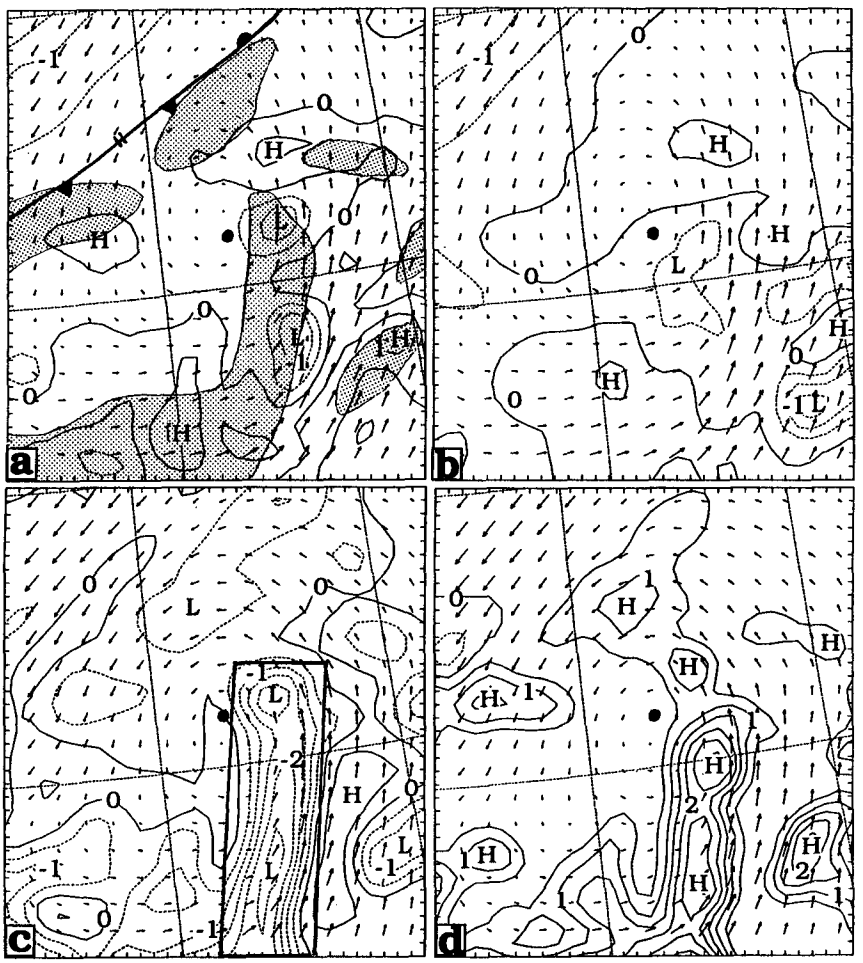

FIG. 13. Horizontal maps of the potential temperature (θ) budget at intervals of 0.5°C h^{-1} at 900 hPa from 72-h simulation (22/12-72): (a) the local θ tendency ($\partial\theta/\partial t$); (b) horizontal advection ($-\mathbf{V}\cdot\nabla\theta$); (c) vertical advection ($-\omega\partial\theta/\partial p$); and (d) parameterized convection ($\partial\theta/\partial t|_{CON}$). Superposed are wind vectors at 900 hPa plotted at every other point (1 grid length represents 18 m s^{-1}) except for (c) and (d) in which system-relative winds are plotted. Solid (dashed) lines are positive (negative) tendencies. Solid circle denotes the surface cyclone center. The surface frontal position and the convective distribution, as shaded, are given in (a). The box given in (c) denotes the averaging area used for composite θ and θ_e budget calculations shown in Figs. 14 and 17, respectively.

13a,b and 12), although they are weak due to the slow transformation. Over the convective region, the diabatic heating and vertical adiabatic cooling dominate the budget but with opposite signs (Figs. 13c,d). In general, the θ tendency is determined by subsidence warming immediately to the east of the convective band, horizontal advection associated with the thermal anomalies around the cyclone center (cf. Figs. 13b and 12b), and the small difference between the convective heating and vertical advection inside the storm. Consequently, it produces net cooling along the north–south-oriented convective region and an elongated zone of net warming along the westerly to southwesterly jet. It is of interest to note that this warming pattern resembles well the distribution of deep convection at 23/00-84 (cf. Figs. 13a and 1d). This appears to suggest that the subsidence warming tends to suppress momentarily convective development, but it contributes to the conditioning of the convective environment for the organization of the oceanic storm as the warmer air is advected northeastward by the low-level jet.

Figure 14 displays vertical composite profiles of all the θ budget terms that are obtained by averaging them roughly along the convective band at 22/12-72. The θ budget above 950 hPa is again nearly balanced by the convective heating and the adiabatic cooling in mesoscale ascent, which are roughly symmetric with their peaks ($\pm$2.5–3 K h^{-1}) at 400 hPa. This large cancellation between the convective heating and vertical advection has also been noted by Kuo and Anthes (1984)

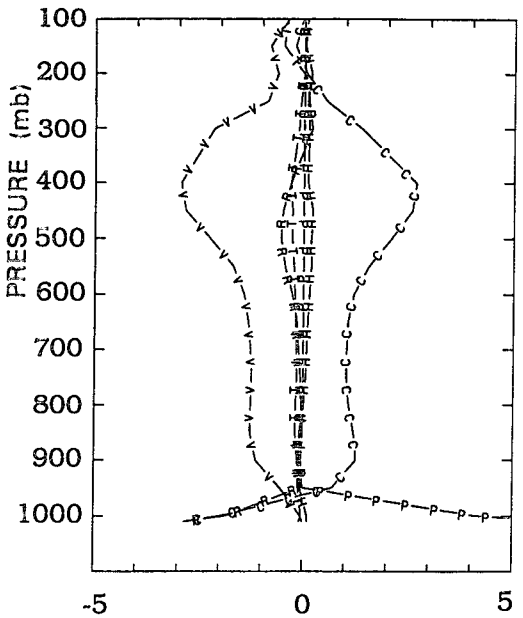

FIG. 14. Vertical composite profiles of the potential temperature θ budget terms (K h^{-1}) at 22/12-72 that are obtained by averaging them over a box as given in Fig. 13c. Letter "T" denotes the local θ tendency ($\partial\theta/\partial t$); "H" the horizontal advection ($-\mathbf{V}\cdot\nabla\theta$); "V" the vertical advection ($-\omega\partial\theta/\partial p$); "C" the parameterized convection ($\partial\theta/\partial t|_{CON}$); "P" the PBL process; and "R" the grid-scale evaporation plus radiative cooling effect.

in their observational budget study of a midlatitude MCS. Parameterized downdrafts, grid-scale evaporation, and cloud-radiation interaction all contribute to the cooling of the PBL, as expected. It is remarkable that this collective cooling is completely offset by the upward transfer of surface sensible heat flux over the warm Gulf Stream water; it occurs at a rate of greater than 6°C h^{-1} at the surface! This explains why little cooling appears in the lowest layers along the oceanic storm (see Figs. 1 and 5), despite the rapid expansion of the convective system. Such a scenario has been observed by Zipser (1977) during the passage of a tropical squall line over warm ocean and by Emanuel et al. (1993) during the transformation of MCSs into tropical cyclones. This is in significant contrast to its continental counterpart in which moist downdrafts are crucial in the generation of new convection and in the propagation of the MCSs (see Zhang and Fritsch 1988). Note, however, that more marked upward flux transfer occurs only in the lowest 50–80 hPa. This implies that the surface fluxes alone could not account for the diminishing of a deep (200–300 hPa) cold pool, unless it is located over a very warm water surface and coupled with intense surface winds over the core region.

One may note that the composite θ tendency shows a deep layer of net cooling, though small, along the convective band, as can also be visualized from Fig. 13a. According to Yanai et al. (1973), the troposphere should be heated in the presence of deep convection; the total warming depends on the amount of precipitation reaching the surface minus radiative cooling. It is found in the present case that the θ tendency does show a deep layer of net warming, mostly associated with compensating subsidence, with the peak rates (about 0.25°C h^{-1}) at 900 and 300 hPa, when the θ budget is evaluated over a much larger area to the east (e.g., see Fig. 13a). This warming effect can be further seen by comparing the 84-h simulations between experiments CTL and NLH (cf. Figs. 12c and 15). Without deep convection, the cold pool and the warm air mass to its east at 22/00-60 (see Fig. 12a) tend to be advected northeastward away from the trough's base, thus resulting in an elongated warm tongue along the southwesterly jetlike flow (Fig. 15). The net (direct and indirect) integral effect of deep convection gives rise to the lower tropospheric warming by 4°–5°C along but slightly to the east of the convective storm (again associated with the subsidence warming), which is in qualitative agreement with the above θ budget calculation. It should be noted that some portion of the warming is caused by horizontal advection of tropical air in the presence of enhanced southwesterly flow in the control simulation.

Figure 16 shows the θ_e budget at 22/12-72 corresponding to the θ budget given in Fig. 13. Like in the θ budget, the θ_e tendency inside the convective storm is also dominated by the parameterized convection and vertical advection (Figs. 16c,d); but they are opposite in sign to their counterparts due to the inverse sign of θ and θ_e gradients in the vertical. With the θ-budget results in mind, we can see that vertical motion along the convective storm tends to transport moisture upward, whereas the parameterized convection removes it as precipitation reaching the surface. Unlike in the θ budget, however, the horizontal θ_e advection (mainly through moisture) accounts for a large percentage of high θ_e along the low-level jet, as well as at the leading edge of the high-θ_e tongue (Fig. 16b). Thus, the horizontal θ_e advection plays an important role in vertically

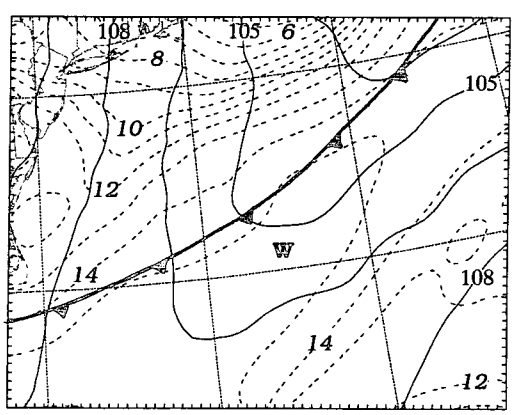

FIG. 15. As in Fig. 12c but from experiment NLH (i.e., no latent heating).

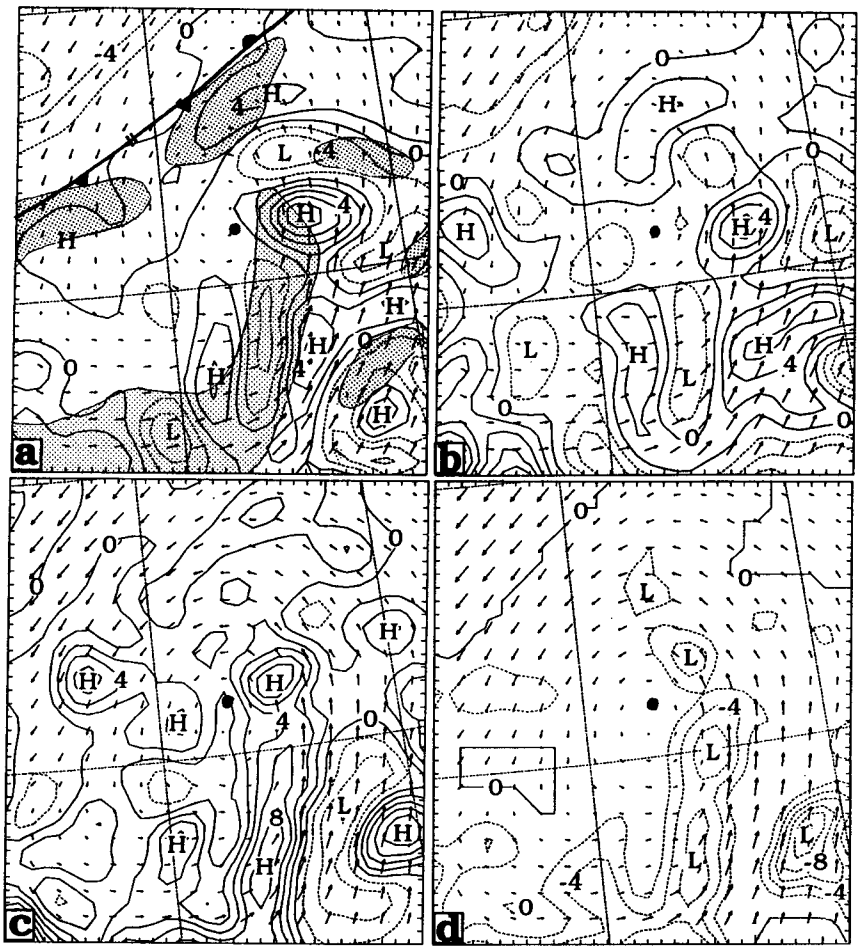

FIG. 16. As in Fig. 13 but for the equivalent potential temperature θ_e budget at intervals of 2 K h^{-1}.

destabilizing atmospheric columns, especially at the leading edge, and spreading deep convection along the low-level jet, as mentioned in Part I. The net result is an increase of θ_e along and immediately to the east of the convective band, which is consistent with the generation of a high-θ_e tongue along the low-level jet (cf. Figs. 11c and 13c in Part I and Fig. 16a herein).

Vertical composite profiles of the θ_e budget terms, given in Fig. 17, exhibit (i) the important vertical stabilization of the troposphere by deep convection; (ii) the marked upward transport of high-θ_e air up to 600 hPa by mesoscale ascent (maximized near 900 hPa); and (iii) the significant role of horizontal transport of high-θ_e air from lower latitudes (peaked in the 800–700-hPa layer) compared to its counterpart in the θ budget (cf. Figs. 15 and 17). Evaporation of grid-scale condensate in the lower-level clouds also contributes positively to the θ_e tendency. Like in the composite θ budget, the air–sea interaction (Emanuel 1986; Rotunno and Emanuel 1987), that is, the upward transfer of surface sensible and latent heat fluxes from the warm Gulf Stream water, is the major process to balance the convective cooling/drying effects (and horizontal advection) in the PBL; both are about 10 K h^{-1} at the surface but opposite in sign. The net θ_e tendency shows a deep layer of moistening in the troposphere, maximized at 800 hPa, along the convective band. It is evident that the slantwise wrapping-around of high-θ_e air above 900 hPa is mainly caused by the horizontal and vertical advection offsetting the convective cooling/drying. Again, the composite net θ_e tendency would be more pronounced if the averaging area is taken slightly to the east of the convective band (Fig. 16a). This increased tendency results primarily from the horizontal advection of higher moisture content from lower latitudes (offset by the descending drying effect, see Figs. 16a–c). It should be noted that while the grid-scale slantwise transport outweighs the boundary layer process above 900 hPa, it is the latter which transfers the necessary high-θ_e air to the top of the PBL for the grid-scale advection to take over.

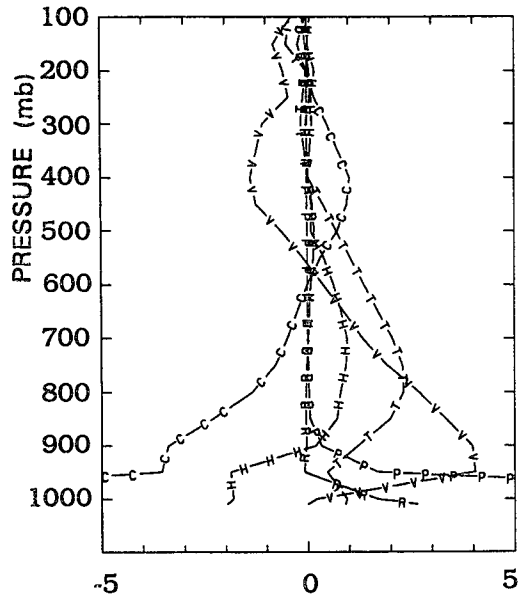

FIG. 17. As in Fig. 14 but for the equivalent potential temperature θ_e budget terms (K h^{-1}).

6. Summary and conclusions

In this paper, we have examined the meso-β-scale structures and evolution of intense cyclonic vorticity and the transformation of a low-level cold pool to a warm-core anomaly associated with an oceanic cyclone/storm system, based on a 90-h real-data simulation of the long-lived MCSs that produced the July 1977 Johnstown flash flood. Model diagnosis has been performed to investigate how the oceanic cyclogenesis occurs at the south periphery of the dissipated MCS in relation to the large-scale environment, the convectively generated vortex/trough, and a new convective storm, after the system drifts into the Atlantic Ocean. Then, budgets of relative vorticity, potential temperature θ, and equivalent potential temperature θ_e have been carried out to gain insight into various dynamical and thermodynamic processes leading to the oceanic cyclogenesis.

It is shown that a surface mesotrough at the end of the continental MCC's life cycle can be related to a midlevel short-wave trough that is characterized by a warm anomaly above and a cold anomaly below. Associated with the surface to midlevel trough is a deep and vertically coherent mesovortex that is accompanied by weak ascent ahead and weak descent behind. The vortex/trough system is shown to be capably *maintained for over 60 h* within a weak-sheared environment, which is the key to the successful prediction of the subsequent oceanic cyclone/storm development. As the vortex/trough moves into the warm Gulf Stream water at lower latitudes, its low-level pressure gradients in the southern quadrants intensify, giving rise to the enhanced mass and moisture convergence in the maritime boundary layer and the development of a new MCS at the southern periphery of the previously dissipated MCC. Then, the new MCS strengthens over the warm ocean surface. Vertical transfer of surface fluxes from the warm ocean in the presence of intensifying surface winds, relayed by their transport in mesoscale updrafts, outperforms the convective drying and cooling, resulting in the generation of a low-level high-θ_e tongue along the elongated convective storm. Meanwhile, stretching of the planetary vorticity plus the residue of the vortex's relative vorticity assists the formation of a cyclonic (shear) vorticity band along the new MCS. A first closed isobar of the surface cyclone appears at the southern periphery of the trough/vortex, as the shear vorticity is advected northward into a weak-gradient region and then converted to curvature vorticity.

Figure 18 provides a conceptual model showing the subsequent wrapping-around of both the vorticity band and high-θ_e tongue along the oceanic storm into the vicinity of the surface cyclone during the intensifying stages. The slantwise wrapping-around of low-level high-θ_e air, through the air–sea interaction and three-dimensional advection, tends to cause conditional instability and *further organization of the oceanic storm* (into a comma-shaped distribution) along a low-level jet. Meanwhile, the vorticity band, wrapping around

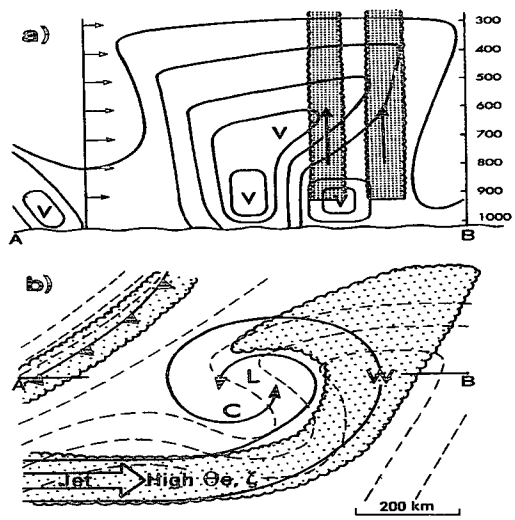

FIG. 18. A conceptual model of the oceanic cyclogenesis during its intensifying stage, showing the wrapping around of high-θ_e air and relative vorticity along a low-level jet, the transition in transforming a low-level cold pool to a warm-core anomaly, and the relationship between the midlevel mesovortex and the low-level cyclonic amplification: (a) vertical cross section of relative vorticity taken through the cyclone center and the vertical shear of the ambient flow is given by arrows to the left; and (b) horizontal map of the low-level system-relative flow (arrows) and temperature (dashed). The scalloped denotes the distribution of deep convection along the oceanic storm. Letters "V," "L," "W(C)" denote the centers of cyclonic vorticity, the surface cyclone, and warm (cold) air, respectively.

toward the cyclone center, is enhanced further by stretching of absolute vorticity in the presence of intensifying flows, leading to the formation of a comma vortex as the shear-curvature vorticity conversion continues. Because of the nonconcentric phase difference between the trough/vortex and the new cyclone, the intensifying cyclonic flow, which overpowers quickly the low-level circulation of the trough/vortex, destroys gradually the vortex's cold pool by advecting the associated cold air mass in the cyclonic northerly flow into the oceanic storm and the ambient warmer air into the cyclone. These processes cause *the transformation of the low-level cold anomaly to a warm-cored structure* near the cyclone center and *the pronounced concentration of cyclonic vorticity,* thus the rapid spinup of the surface cyclone to tropical-storm intensity; it deepens 14 hPa in 24 h. It is shown that the convectively generated vorticity anomaly determines the amplification and propagation of the surface cyclone as well as the low-level thermodynamic transformation.

It is found that the convectively generated mesovortex from the previous MCSs makes little direct contribution, that is, through vertical advection, to the generation of the low-level intense cyclonic vorticity. We have shown that the roles of the mesovortex in the cyclogenesis are to (i) provide a favorable meso-α-scale environment with a broad, vertically coherent, cyclonic circulation and a deep high-θ_e layer in the midtroposphere; (ii) assist the initial organization of deep convection through the enhanced boundary layer convergence and the increased upward surface fluxes in the presence of intensifying low-level flows (see section 5 of Part I) over the warm ocean; and (iii) supply the necessary cyclonic vorticity to stretch along the convectively enhanced convergence zone. Once the new cyclonic circulation is established, however, the midlevel vortex, centered in the wake of the oceanic storm, tends to have less significant impact on the surface cyclogenesis but intensify slowly in the convective region through the stretching of absolute vorticity (as illustrated in Fig. 18a).

In conclusion, we may state that the midlevel mesovortex, as it moves toward the warm Gulf Stream water, provides the necessary forcing for the initiation and organization of deep convection and for the initial concentration of low-level cyclonic vorticity at its southern periphery, whereas the new convective system contributes to the amplification of the low-level cyclonic vorticity through stretching in the presence of intensifying flow and then the storm-cyclone interaction eliminates the low-level cold anomaly, thereby accomplishing the transformation of the continental MCS/vortex system to the intense oceanic cyclone/storm system. It takes 24 h to get the oceanic storm organized and another 24 h to complete the thermodynamic transformation. Sensitivities of the model-simulated cyclogenesis to the midlevel mesovortex, air–sea interaction, cloud–radiation interaction, and other physical processes will be examined in a forthcoming article of this series of papers.

It should be noted, though, that the above conclusions are only obtained from a single case study in which numerous physical processes are parameterized and little upper-air observations were available for verification. Nevertheless, because there are so many similarities between the observed and simulated scenarios, we believe that the results presented herein are relevant to tropical (or barotropic) cyclogenesis from MCSs. In particular, we have shown that many mesoscale structures and evolutionary features of the cyclogenesis presented above are similar to those in previous tropical cyclogenesis studies, and to those observed at the early stages of tropical cyclogenesis during TEXMEX. They include the convectively generated midlevel mesovortex associated with a short-wave trough, the vertical warm–cold anomaly couplet, the generation of high-vorticity bands at some distance from the midlevel mesovortex, the formation of a low-level comma vortex, little surface cooling beneath convective cloud clusters, and the transformation of the low-level cold anomaly to a warm-core structure during the rapid genesis stages. The evolution of the present oceanic cyclone with respect to the large-scale baroclinic system near the end of the 90-h integration also provides some interesting information on the interaction of tropical storms with baroclinic waves as they move to midlatitudes.

Acknowledgments. We are grateful to two anonymous reviewers whose comments help improve significantly the presentation of our results. The computations were performed on the CRAY Y-MP (Shavano) at the National Center for Atmospheric Research (NCAR) under Grant ATM-92-22017. NCAR is sponsored by the National Science Foundation. This research was supported by Natural Sciences and Engineering Research Council of Canada.

APPENDIX

Conversion between Shear and Curvature Vorticity

The intensification of curvature vorticity through the conversion processes can be simply demonstrated by applying the curvature vorticity equation, after neglecting all terms coupled with divergence as well as the tilting term in Eqs. (2.7a) and (2.16) of Bell and Keyser (1993), to the flows in the vicinity of the cyclone center (see Figs. 5b and 10). That is,

$$\frac{d}{dt}\left(V\frac{\partial\alpha}{\partial s}\right) = V^2\frac{\partial K_t}{\partial s} - K_s\frac{\partial\phi}{\partial s}, \qquad \text{(A1)}$$

where $V\partial\alpha/\partial s$ is the curvature vorticity; ϕ is the geopotential height; and K_t and K_s are the parcel trajectory curvature and streamline curvature, respectively. Both terms on the rhs of Eq. (A1) represent conversions between curvature and shear vorticity. The first term re-

sults from alongstream variations in parcel trajectory curvature weighted by V^2, while the second term denotes cross-contour flow in the presence of streamline curvature.

It is apparent that the two terms on the rhs are positive along both the trajectories and streamlines close to the cyclone center, thus allowing the conversion of shear to curvature vorticity as air parcels with considerable shear vorticity wrap around toward the center (i.e., with increasing curvature and cross-isobaric flow). During the incipient stages of the cyclogenesis, the second term is generally small because the pressure gradients in the northeast quadrant are very weak (see Fig. 1b). Thus, the conversion of shear to curvature vorticity takes place mainly due to the rapidly increased curvatures along the parcels' trajectories. It should be pointed out that the curvature vorticity can also intensify rapidly through vortex stretching in the presence of strong convergence [see Eq. (2.7a) in Bell and Keyser (1993)]. In the present case, this occurs near the leading portion of the convective V-band where strong convergence is present, and it is more pronounced at later stages, that is, after 22/12-72, when both local curvature vorticity and convergence are intense over the comma head portion of the storm (see Fig. 11). This can also be inferred from the vorticity budgets discussed in section 4.

REFERENCES

Anthes, R. A., E. -Y. Hsie, and Y. -H. Kuo, 1987: Description of the Penn State/NCAR mesoscale model version 4 (MM4). NCAR Tech. Note NCAR/TN-282, 66 pp. [Available from NCAR, P.O. Box 3000, Boulder, CO 80307.]

Bell, G. D., and D. Keyser, 1993: Shear and curvature vorticity and potential-vorticity interchanges: Interpretation and application to a cutoff cyclone event. *Mon. Wea. Rev.*, **121,** 76–102.

Bister, M., and K. A. Emanuel, 1994: Observations of tropical cyclogenesis in TEXMEX. Preprints, *Sixth Conf. Mesoscale Processes,* Portland, OR, Amer. Meteor. Soc., 53–56.

Bosart, L. R., and F. Sanders, 1981: The Johnstown flood of July 1977: A long-lived convective storm. *J. Atmos. Sci.,* **38,** 1616–1642.

Davidson, N. E., G. I. Holland, J. L. McBride, and T. D. Keenan, 1990: On the formation of AMEX tropical cyclones Irma and Jason. *Mon. Wea. Rev.*, **118,** 1981–2000.

Emanuel, K. A., 1986: An air–sea interaction theory for tropical cyclones. Part I: Steady state maintenance. *J. Atmos. Sci.,* **43,** 585–604.

——, N. Renno, L. R. Schade, M. Bister, M. Morgan, D. Raymond, and R. Rotunno, 1993: Tropical cyclogenesis over the eastern North Pacific: Some results of TEXMEX. Preprints, *20th Conf. Hurricanes and Tropical Meteorology,* San Antonio, TX, Amer. Meteor. Soc., 110–113.

Frank, W. M., 1977: The structure and energetics of the tropical cyclone. Part I: Storm structure. *Mon. Wea. Rev.*, **105,** 1119–1135.

Fritsch, J. M., J. D. Murphy, and J. S. Kain, 1994: Warm-core vortex amplification over land. *J. Atmos. Sci.,* **51,** 1780–1807.

Houze, R. A., Jr., 1989: Observed structure of mesoscale convective systems and implications for large-scale heating. *Quart. J. Roy. Meteor. Soc.,* **115,** 425–461.

Kain, J. S., and J. M. Fritsch, 1990: A one-dimensional entraining/detraining plume model and its application in convective parameterization. *J. Atmos. Sci.,* **47,** 2784–2802.

——, and ——, 1994: Convective parameterization for mesoscale models: The Kain–Fritsch scheme. *The Representation of Cumulus Convection in Numerical Models, Meteor. Monogr.,* No. 46, Amer. Meteor. Soc., 165–170.

Kuo, Y.-H., and R. A. Anthes, 1984: Mesoscale budgets of heat and moisture in a convective system over the central United States. *Mon. Wea. Rev.,* **112,** 1482–1497.

Lopez, L., D. Raymond, and K. Emanuel, 1993: Preliminary results from TEXMEX: The development of tropical storm Guillermo. Preprints, *20th Conf. Hurricanes and Tropical Meteorology,* San Antonio, TX, Amer. Meteor. Soc., 114–117.

Mapes, B. E., and R. A. Houze Jr., 1993: An integrated view of the 1987 Australia monsoon and its mesoscale convective systems. Part II: Vertical structure. *Quart. J. Roy. Meteor. Soc.,* **119,** 733–754.

Raymond, D. J., and H. Jiang, 1990: A theory for long-lived mesoscale convective systems. *J. Atmos. Sci.,* **47,** 3067–3077.

Rotunno, R., and K. A. Emanuel, 1987: An air–sea interaction theory for tropical cyclones. Part II: Evolutionary study using a nonhydrostatic axisymmetric numerical model. *J. Atmos. Sci.,* **44,** 542–561.

Tuleya, R. E., and Y. Kurihara, 1984: The formation of comma vortices in a tropical numerical simulation model. *Mon. Wea. Rev.,* **112,** 491–502.

Wetzel, P. J., W. R. Cotton, and R. L. McAnelly, 1983: A long-lived mesoscale convective complex. Part II: Evolution and structure of the mature complex. *Mon. Wea. Rev.,* **111,** 1919–1937.

Yanai, M., S. Esbensen, and J. Chu, 1973: Determination of bulk properties of tropical cloud clusters from large-scale heat and moisture budgets. *J. Atmos. Sci.,* **30,** 611–627.

Zehr, R. M., 1992: Tropical cyclogenesis in the western North Pacific. NOAA Tech. Rep. NESDIS 61, NOAA/NESDIS, Washington, DC, 181 pp.

Zhang, D.-L., 1989: The effect of parameterized ice microphysics on the simulation of vortex circulation with a mesoscale hydrostatic model. *Tellus,* **41A,** 132–147.

——, and J. M. Fritsch, 1986: Numerical simulation of the meso-β-scale structure and evolution of the 1977 Johnstown flood. Part I: Model description and verification. *J. Atmos. Sci.,* **43,** 1913–1943.

——, and ——, 1987: Numerical simulation of the meso-β-scale structure and evolution of the 1977 Johnstown flood. Part II: Inertially stable warm-core vortex and the mesoscale convective complex. *J. Atmos. Sci.,* **44,** 2593–2612.

——, and ——, 1988: Numerical sensitivity experiments of varying model physics on the structure, evolution and dynamic of two mesoscale convective systems. *J. Atmos. Sci.,* **45,** 261–293.

——, and N. Bao, 1996: Oceanic cyclogenesis as induced by a mesoscale convective system moving offshore. Part I: A 90-h real-data simulation. *Mon. Wea. Rev.,* **124,** 1449–1469.

——, E.-Y. Hsie, and M. W. Moncrieff, 1988: A comparison of explicit and implicit prediction of convective and stratiform precipitating weather systems with a meso-β-scale numerical model. *Quart. J. Roy. Meteor. Soc.,* **114,** 31–60.

Zipser, E. J., 1977: Mesoscale and convective-scale downdrafts as distinct components of squall-line structure. *Mon. Wea. Rev.,* **105,** 1568–1589.